

1 **Thermo-Economic and Environmental Optimization of a**
2 **Solar-driven Zero-Liquid Discharge System for Shale Gas**
3 **Wastewater Desalination**

4
5
6 Viviani C. Onishi ^{a, *}, Mohammad H. Khoshgoftar Manesh ^{b, c}, Raquel Salcedo-Díaz ^d,
7 Rubén Ruiz-Femenia ^d, Juan A. Labarta ^d, José A. Caballero ^d

8
9
10 ^a *School of Engineering and the Built Environment, Edinburgh Napier University, 10*
11 *Colinton Road, Edinburgh EH10 5DT, UK*

12 ^b *Energy, Environment and Biologic Research Lab (EEBRlab), Division of Thermal Sciences*
13 *and Energy Systems, Department of Mechanical Engineering, Faculty of Technology &*
14 *Engineering, University of Qom, Qom, Iran*

15 ^c *Center of Environmental Research, Qom, Iran*

16 ^d *Institute of Chemical Process Engineering, University of Alicante, BO-03080, Alicante,*
17 *Spain*

18
19
20
21
22
23
24 *** Corresponding author at.**

25 *School of Engineering and the Built Environment, Edinburgh Napier University, 10 Colinton*
26 *Road, Edinburgh EH10 5DT, UK. Email address: V.Onishi@napier.ac.uk (Viviani C. Onishi)*

1 **ABSTRACT**

2 Wastewater management is one of the main hurdles encountered by the shale
3 gas industry for boosting overall process cost-effectiveness while reducing
4 environmental impacts. In this light, this paper introduces a new multi-objective
5 model for the thermo-economic and environmental optimization of solar-based
6 zero-liquid discharge (ZLD) desalination systems. The solar-driven ZLD system is
7 especially developed for desalinating high-salinity wastewaters from shale gas
8 process. A decentralized system is proposed, encompassing a solar thermal
9 system, a Rankine power cycle, and a multiple-effect evaporator combined with
10 mechanical vapor recompression. The environment-friendly ZLD operation is
11 ensured by specifying the salt concentration of brine discharges close to
12 saturation conditions. The mathematical modelling approach is centered on a
13 multi-objective non-linear programming (MoNLP) formulation, which is aimed at
14 simultaneously minimizing thermo-economic and environmental objective
15 functions. The latter objective function is quantified by the ReCiPe methodology
16 based on life cycle assessment. The MoNLP model is implemented in GAMS
17 software, and solved through the epsilon-constraint method. A set of trade-off
18 Pareto-optimal solutions is presented to support decision-makers towards
19 implementing more sustainable and cost-efficient solar-driven ZLD desalination
20 systems. The comprehensive energy, economic and environmental analysis
21 reveals that the innovative system significantly decreases costs and
22 environmental impacts in shale gas wastewater operations.

23

24 **Keywords:** Optimization, shale gas wastewater, high-salinity wastewater, zero-
25 liquid discharge, multiple-effect evaporation, mechanical vapor recompression,
26 renewable energy.

1 **1. Introduction**

2 Advances in horizontal drilling and hydraulic fracturing technologies allied to
3 supportive policies have fueled large-scale shale gas exploration worldwide
4 throughout the last decade. Notwithstanding, the intensification in shale gas
5 production around the world has also fostered concerns about adverse effects on
6 communities, public health and the environment. The environmental impacts are
7 mainly associated with the depletion of water resources and wastewater pollution
8 [1–3], induced seismic events [4], and greenhouse gas (GHG) emissions [5].
9 Regarding the water-related implications, the gas extraction process from tight
10 shale reservoirs usually requires significant volumes of water and generates
11 excessive amounts of high-salinity wastewater [6,7]. As a result, wastewater
12 management is one of the main obstacles faced by the shale gas industry to
13 improve overall cost-effectiveness and reduce environmental impacts [8,9].

14 In shale gas operations, thermal desalination systems based on multiple-
15 effect evaporation with mechanical vapor recompression (MEE-MVR) provide a
16 viable solution for the zero-liquid discharge (ZLD) treatment of high-salinity
17 wastewaters from gas extraction. Onishi et al. [10] have developed a non-linear
18 programming (NLP) model for the systematic optimization of ZLD desalination
19 processes. The authors have carried out a thorough comparison of several system
20 configurations –single/multiple-effect evaporation (SEE/MEE) with/without
21 multistage compression and thermal integration– in terms of producing
22 freshwater and achieving ZLD conditions under different inlet conditions. Their
23 comprehensive energy and economic analysis have shown that the MEE-MVR
24 system is the most cost-effective process for the ZLD desalination of shale gas
25 wastewater. The authors have estimated desalination treatment costs ranging
26 from 6.7–10.9 US\$/m³ (without brine disposal expenses) depending on the
27 system configuration, while wastewater disposal costs in conventional Class II
28 saline water injection wells are projected to be between 8–25 US\$/m³ [8,11]. In

1 Onishi et al. [12], the authors have extended their previous modelling approach
2 to allow for evaluating the most important geometrical features of the
3 desalination system during the optimization task. Their improved rigorous model
4 has also highlighted the ability of ZLD-MEE-MVR desalination for the economic
5 and effective treatment of shale gas wastewaters.

6 For addressing the uncertainty associated with shale gas wastewater data,
7 Onishi et al. [13] have introduced a stochastic multiscenario NLP-based model for
8 the optimal design of ZLD desalination systems. In this approach, the authors
9 have considered both wastewater salinity and flowrate as uncertain design
10 parameters to enhance system flexibility and reliability. Thus, the latter uncertain
11 parameters have been modelled as a set of correlated feeding water scenarios
12 with a given probability of occurrence. The authors have presented cumulative
13 probability curves to appraise the economic risk linked to the uncertain space for
14 distinct standard deviations of expected mean values. Their results reveal that the
15 proposed stochastic multiscenario approach leads to improved thermo-economic
16 performance solutions in comparison to previous deterministic models.

17 Although aforementioned studies have highlighted the feasibility of ZLD-
18 MEE-MVR desalination systems for reducing wastewater impacts while improving
19 water resources in shale gas operations, their practical implementation is still
20 restricted by their intensive energy consumption and associated pollutant carbon
21 emissions. For instance, the SEE/MEE-MVR technologies for ZLD desalination
22 developed in Onishi et al. [10] have presented specific energy consumption
23 ranging from 28–50.5 kWh_e per cubic meter of produced freshwater. According
24 to the US Energy Information Administration [14], about 939 g/kWh_e of CO₂ are
25 generated to produce electricity from burning coal. Under the latter assumption,
26 the referred SEE/MEE-MVR systems operating at ZLD conditions would yield to
27 ~26–47 kg of CO₂ per cubic meter of produced freshwater [8,10]. These results
28 emphasize the need for developing more sustainable alternatives for ZLD

1 desalination systems, particularly involving the integration of renewable energy
2 resources.

3 The integration of solar thermal energy to power desalination systems has
4 attracted increased interest from the literature over the past few years. Into this
5 framework, Pouyfaucou and García-Rodríguez [15] have studied different solar
6 thermal-powered desalination technologies to identify main issues for improving
7 market opportunities. The authors have presented a thorough performance and
8 economic analysis of distinct membrane distillation (MD) and reverse osmosis
9 (RO)-based desalination systems assisted by solar photovoltaic and solar thermal
10 power plants. Their analysis has included parabolic trough collectors, linear
11 Fresnel concentrators, and dish concentrators. Moore et al. [16] have examined
12 the coupling of thermal solar thermal collectors to sweeping-gas MD systems via
13 economic optimization. Karanikola et al. [17] have also provided an economic
14 performance evaluation of MD desalination system driven by solar photovoltaic
15 and solar thermal collectors. Zheng and Hatzell [18] have developed a techno-
16 economic model to evaluate the viability of combining solar collectors with
17 multistage flash distillation (MSF) systems. Their model accounts for several
18 factors such as system lifetime and scale, performance parameters of different
19 system units, and payback period, aimed at surpassing geographic and technical
20 constraints.

21 Aboelmaaref et al. [19] have presented a comprehensive review on
22 concentrated solar power (CSP) desalination technologies. The authors have paid
23 particular attention on the thermodynamic and economic analysis of desalination
24 systems driven by parabolic trough collectors and parabolic dish CSP
25 technologies. Ghenai et al. [20] have proposed an optimization approach based
26 on response surface for improving hybrid multi-effect distillation (MED) and
27 adsorption desalination (AD) systems powered by solar thermal energy. Their
28 optimization method, along with performance analysis and parametric study, are
29 used to identify the optimal operating conditions to increase the freshwater

1 production while reducing energy consumption. Even though previous studies
2 have presented insightful results on the integration of solar thermal technologies
3 to desalination plants, none of them have considered ZLD processes. To tackle
4 this issue, Najaf et al. [21] have performed a thermo-economic evaluation of a
5 ZLD desalination plant equipped with parabolic trough solar collectors. Their
6 simulation model approach is focused on an industrial wastewater treatment
7 plant composed of a brine concentrator and a forced-circulation crystallizer.
8 However, their approach disregards energy intensive high-salinity applications, as
9 well as the assessment of environmental impacts of the process.

10 To overcome shortcomings in preceding research, this paper introduces a
11 new multi-objective modelling approach for the thermo-economic and
12 environmental optimization of solar-driven ZLD desalination systems. The multi-
13 objective model is developed by considering a multistage superstructure that
14 includes a solar thermal system (STS), a Rankine cycle (RC) unit, and a MEE-MVR
15 desalination plant. The proposed desalination process is particularly applied for
16 treating high-salinity shale gas wastewaters. A design constraint specifying the
17 salt concentration in brine discharges close to saturation conditions is added to
18 the model to ensure the ZLD operation. Also, the STS is designed to operate in
19 different time periods to account for the intermittency in daily solar irradiance
20 throughout the year. The model is formulated as a multi-objective NLP problem
21 (or MoNLP), which is implemented in GAMS software, and solved via the epsilon-
22 constraint method to minimize both thermo-economic and environmental
23 objective functions. The environmental performance is evaluated by the ReCiPe
24 methodology, which is based on life cycle assessment (LCA) techniques. The
25 proposed methodology allows obtaining a set of alternative Pareto-optimal
26 solutions to support decision-makers towards the implementation of more
27 environment-friendly and cost-effective solar-driven ZLD desalination systems.

28 The rest of this study is structured as follows. **Section 2** briefly introduces
29 the problem statement of multi-objective optimization of solar-driven ZLD

1 desalination systems. The process description of the ZLD-MEE-MVR desalination
2 plant, and RC and STS units are presented in **Section 3**. In **Section 4**, the multi-
3 objective modelling approach is developed. The illustrative case study used to
4 assess the applicability of the proposed model is described in **Section 5**, whilst
5 the main results obtained are discussed in **Section 6**. Finally, the major
6 conclusions are summarized in **Section 7**.

7

8 **2. Problem Statement**

9 The multi-objective optimization problem can be formally stated as follows. Given
10 is a set of inlet feed water (*i.e.*, high-salinity shale gas wastewater) conditions
11 (which include temperature, salinity, and mass flowrate), and the ZLD target state.
12 The technical characteristics of the MEE-MVR system, Rankine cycle units, and
13 solar parabolic trough collectors are also known, along with weather conditions,
14 economic, and environmental impact data. Utilities (electricity, cooling water and
15 natural gas) are available, and their related prices and environmental data are
16 known. The main goal is to obtain an optimal design and operating conditions
17 for the solar-based ZLD-MEE-MVR desalination system that simultaneously
18 enhance its thermal-economic and environmental performances. To do so, a
19 multi-objective NLP-based model is developed and solved via the epsilon-
20 constraint method, through the minimization of the economic and environmental
21 objective functions. In this approach, the STS should follow a multi-period
22 operation to account for the different weather conditions throughout the year. In
23 addition, the ZLD plant operation is safeguarded by considering a design
24 restriction that sets the discharge salinity close to the salt saturation condition.
25 The process description is presented as follows.

26

27

1 **3. Process Description**

2 For the analysis, an integrated system is considered which is composed of a MEE-
3 MVR desalination plant, STS, and Rankine cycle unit. The schematic diagram for
4 the solar-based ZLD desalination system is displayed in **Fig. 1**.

5 6 **3.1. ZLD Thermal Desalination System**

7 The proposed ZLD-MEE-MVR desalination system is composed of a multiple-
8 effect evaporator under a horizontal-tube configuration, which is coupled to
9 intermediate flashing tanks for enhancing energy recovery efficiency. In the
10 system, a feeding-distillate preheater is also used to further increase the thermal
11 integration, whilst the vapor produced by flashing and evaporation processes are
12 managed by a mechanical compressor. Further details on the design and
13 operation of MEE-MVR desalination systems are presented in the author's
14 previous studies [10,12,13].

15

16 **3.2. Solar-Assisted Thermal System**

17 The STS is comprised by a solar field of parabolic trough collectors, in which the
18 solar thermal energy is transferred to the thermal operating fluid (*i.e.*, mineral oil).
19 A backup natural gas-fired heater (GFH) is used to meet the energy shortages
20 that could result from the daily solar intermittency. The GFH ensures the constant
21 energy supply to the MEE-MVR desalination plant, by keeping the thermal
22 operating fluid of the STS at constant temperature.

23

24 **3.3. Steam Rankine Power Cycle**

25 The steam Rankine power cycle comprises a steam turbine, a condenser, a pump,
26 and a boiler (heat exchanger). The Rankine cycle unit is used to convert the solar
27 energy from the STS into the electric power required by the mechanical vapor
28 compressor in the MEE-MVR desalination plant. In this cycle, the working fluid

1 (water) exchanges heat with the thermal solar fluid of the STS in the boiler to
2 produce hot steam. Then, the hot steam is used to produce electricity by passing
3 through the turbine generator. The humid vapor from the turbine exchanges heat
4 with cooling water in the condenser before being pumped back towards the
5 boiler where the power cycle is restarted.

6

7 **4. Multi-Objective Optimization Model**

8 The multi-objective mathematical model for the optimal design and operation of
9 solar-driven ZLD thermal desalination systems is developed through an NLP-
10 based formulation. The optimization approach encompasses the thermodynamic
11 modelling equations of the MEE-MVR desalination plant, steam Rankine cycle,
12 solar thermal collectors' system, and economic and environmental objective
13 functions. The model is built upon the general superstructure as shown in **Fig. 1**.
14 The multi-objective optimization model is presented in the following sections, in
15 which the solar-driven ZLD-MEE-MVR superstructure is generated according to
16 the subsequent steps.

17

18 **4.1. Modelling of the Thermal Desalination System**

19 The mathematical programming model for optimizing the ZLD-MEE-MVR
20 desalination plant comprises energy and mass balances, temperature and
21 pressure feasibility restrictions, along with the ZLD design constraint. The
22 mathematical formulation is based on the author's previous studies concerning
23 the design and optimization of MEE-MVR desalination systems presented in
24 Onishi et al. [10,12,13]. The NLP-based model for the optimal ZLD-MEE-MVR
25 design is presented in the **Appendix A**. The thermodynamic correlations used in
26 the model are shown in the **Appendix B**. In this study, the following assumptions
27 are taken into consideration to simplify the model formulation:

28

- 1 (i) Steady-state operation.
- 2 (ii) Thermal losses in system units are negligible.
- 3 (iii) Vapor streams in evaporator effects are modelled as an ideal gas.
- 4 (iv) Pressure drops in system units are negligible.
- 5 (v) The non-equilibrium allowance (NEA) is negligible.
- 6 (vi) The mechanical compressor operates adiabatically with a known
- 7 isentropic efficiency.
- 8 (vii) The starter power of the mechanical compressor is negligible.
- 9 (viii) Capital costs of mixers are negligible.

10

11 **4.2. Modelling of the Steam Rankine Cycle**

12 The thermal efficiency of the steam Rankine cycle is given by the following
13 equation.

14

$$15 \quad \eta^{RC} = W^{RC} / Q^{Boiler} \quad (1)$$

16

17 In which, W^{RC} represents the net power of the Rankine cycle, while Q^{Boiler}
18 is the thermal power of the boiler. The following inequality constraint is required
19 to couple the steam Rankine cycle to the ZLD-MEE-MVR desalination system.

20

$$21 \quad W^{RC} \geq W^{compressor} \quad (2)$$

22

23 In which, **Eq. (2)** is used to ensure that net power provided by the Rankine
24 cycle is higher or equal to the power needed to drive the compressor in the
25 desalination system. The net power of the Rankine cycle is given as follows.

26

$$27 \quad W^{RC} = W^{turbine} - W^{RC_pump} \quad (3)$$

28

1 In which, $W^{turbine}$ and $W^{RC-pump}$ represent the mechanical power produced
2 by the steam turbine and consumed by the pump in the Rankine cycle,
3 respectively. The modelling equations of the steam turbine, pump, and condenser
4 of the steam Rankine cycle are presented in the next sections.

5 6 4.2.1. Steam Turbine

7 The mechanical power produced by the steam turbine is given by the following
8 equation.

$$9
10 W^{turbine} = \dot{m}^{RC} \cdot (h_{in}^{turbine} - h_{out}^{turbine}) \quad (4)$$

11
12 In **Eq. (4)**, \dot{m}^{RC} indicates the mass flowrate of the working fluid (water) in
13 the Rankine cycle, which is constant throughout the cycle. $h_{in}^{turbine}$ and $h_{out}^{turbine}$ are the
14 specific enthalpies of the working fluid at the inlet and outlet of the turbine,
15 respectively. The specific enthalpy of vapor at the turbine outlet $h_{out}^{turbine}$ is estimated
16 from the definition of isentropic efficiency η^{IS} as follows.

$$17
18 h_{out}^{turbine} = h_{in}^{turbine} - \eta^{IS} \cdot (h_{in}^{turbine} - h_{out}^{IS}) \quad (5)$$

19
20 The isentropic enthalpy of the humid vapor at the turbine outlet is defined
21 as follows.

$$22
23 h_{out}^{IS} = h_{out}^L - x^{IS} \cdot (h_{out}^V - h_{out}^L) \quad (6)$$

24
25 The vapor quality in the isentropic expansion process is given by the
26 following expression.

27

$$x^{IS} = \frac{S_{out}^{turbine} - S_{out}^L}{S_{out}^V - S_{out}^L} \quad (7)$$

2

3 The specific enthalpies and entropies of liquid and vapor states at the
4 turbine outlet are estimated by the following correlations [22,23].

5

$$\begin{cases} h_{out}^L = a_{hL} + b_{hL} \cdot T^{sat} + c_{hL} \cdot (T^{sat})^2 + d_{hL} \cdot (T^{sat})^3 + e_{hL} \cdot (T^{sat})^4 + f_{hL} \cdot (T^{sat})^5 \\ h_{out}^V = a_{hV} + b_{hV} \cdot T^{sat} + c_{hV} \cdot (T^{sat})^2 + d_{hV} \cdot (T^{sat})^3 + e_{hV} \cdot (T^{sat})^4 + f_{hV} \cdot (T^{sat})^5 \end{cases} \quad (8)$$

$$\begin{cases} s_{out}^L = a_{sL} + b_{sL} \cdot T^{sat} + c_{sL} \cdot (T^{sat})^2 + d_{sL} \cdot (T^{sat})^3 + e_{sL} \cdot (T^{sat})^4 + f_{sL} \cdot (T^{sat})^5 \\ s_{out}^V = a_{sV} + b_{sV} \cdot T^{sat} + c_{sV} \cdot (T^{sat})^2 + d_{sV} \cdot (T^{sat})^3 + e_{sV} \cdot (T^{sat})^4 + f_{sV} \cdot (T^{sat})^5 \end{cases} \quad (9)$$

8

9 The following inequality constraints are used to guarantee the temperature
10 and pressure feasibility in the steam turbine.

11

$$\begin{cases} T_{out}^{turbine} \leq T_{in}^{turbine} \\ T_{in}^{turbine} \geq T_{in}^{sat} \\ P_{out}^{sat} \leq P_{in}^{sat} \end{cases} \quad (10)$$

13

14 The pressure of vapor in saturation conditions is obtained from the
15 modified version of the Antoine equation as available in the process simulator
16 Aspen HYSYS.

17

$$P^{sat} = \exp\left(A + \frac{B}{C + T^{sat}} + D \cdot \ln(T^{sat}) + E \cdot (T^{sat})^F\right) \quad (11)$$

19

20 4.2.2. Rankine Cycle Pump

21 The power consumed by the pump in the Rankine cycle is estimated as follows.

22

$$W^{RC_pump} = \frac{\dot{m}^{RC} \cdot v \cdot (P_{in}^{sat} - P_{out}^{sat})}{\eta^{RC_pump}} \quad (12)$$

In which, v represents the specific volume of liquid water, while η^{RC_pump} indicates the RC pump efficiency. The specific enthalpy of the working fluid at the pump outlet is obtained by the following equation.

$$h_{out}^{RC_pump} = h_{in}^{RC_pump} + v \cdot (P_{in}^{sat} - P_{out}^{sat}) \quad (13)$$

Note that the properties at the inlet of the pump should correspond to those at the condenser outlet in the Rankine cycle. Hence, $h_{in}^{RC_pump} = h_{out}^{condenser}$.

4.2.3. Condenser

The thermal power of the condenser in the Rankine cycle is given as follows.

$$Q^{condenser} = \dot{m}^{RC} \cdot (h_{in}^{condenser} - h_{out}^{condenser}) \quad (14)$$

In which, $h_{in}^{condenser}$ and $h_{out}^{condenser}$ are the specific enthalpies of the working fluid at the inlet and outlet of the condenser, respectively. Note that the properties at the inlet of the condenser should correspond to those at the turbine outlet. Hence, $h_{in}^{condenser} = h_{out}^{turbine}$. The heat transfer area of the condensed can be obtained by the following equation.

$$A^{condenser} = \frac{Q^{condenser}}{U^{condenser} \cdot LMTD^{condenser}} \quad (15)$$

In which, $U^{condenser}$ indicates the heat transfer coefficient. The logarithmic mean temperature difference $LMTD^{condenser}$ is obtained through the Chen's

1 approximation (see **Appendix A**) [24]. In this case, the temperature differences
2 are stated as follows.

3

$$4 \quad \begin{cases} \theta_1 = T_{in}^{condenser} - T_{out} \\ \theta_2 = T_{out}^{condenser} - T_{in} \end{cases} \quad (16)$$

5

6 In which,

$$7 \quad \begin{cases} T_{in}^{condenser} \geq T_{out} + \Delta T_{min} \\ T_{out}^{condenser} \geq T_{in} + \Delta T_{min} \end{cases} \quad (17)$$

8

9 The thermal power required by the Rankine cycle to generate hot steam in
10 the boiler outlet is provided by heat exchanges with the working fluid of the STS.
11 The modelling equations for the STS are presented as follows.

12

13 **4.3. Modelling of the Solar Thermal System**

14 The STS is designed to operate in different time periods, which account for the
15 daily solar radiation flux (irradiance) throughout the year. Thus, the following
16 index set is needed to develop the multi-period model for the solar thermal
17 system design.

18

$$19 \quad T = \{t / t = 1, 2, \dots, T \text{ is a time period}\}$$

20

21 The heat demands of the boiler are provided by the solar collectors' field
22 and a backup GFH. Therefore, the global energy balance in the solar thermal
23 system is expressed as follows.

24

$$25 \quad Q_t^{boiler} = Q_t^{SC} + Q_t^{GFH} \quad \forall t \in T \quad (18)$$

26

In which, Q_t^{boiler} , Q_t^{SC} and Q_t^{GFH} refer to the thermal power of the boiler, solar collectors' field, and GFH in the time period $t \in T$, respectively.

The mass balances at each node of the solar thermal system are given by the following formulation (see **Fig. 1**).

$$\begin{cases} \dot{m}_{out,t}^{boiler} = \dot{m}_{in,t}^{SC} + \dot{m}_{in,t}^{GFH} \\ \dot{m}_{in,t}^{boiler} = \dot{m}_{out,t}^{SC} + \dot{m}_{out,t}^{GFH} \\ \dot{m}_{in,t}^{boiler} = \dot{m}_{out,t}^{boiler} \\ \dot{m}_{in,t}^{SC} = \dot{m}_{out,t}^{SC} \\ \dot{m}_{in,t}^{GFH} = \dot{m}_{out,t}^{GFH} \end{cases} \quad \forall t \in T \quad (19)$$

The energy balances at each node of the solar thermal system are given by the following formulation.

$$\begin{cases} \dot{m}_{out,t}^{boiler} \cdot h_{out,t}^{boiler} = \dot{m}_{in,t}^{SC} \cdot h_{in,t}^{SC} + \dot{m}_{in,t}^{GFH} \cdot h_{in,t}^{GFH} \\ \dot{m}_{in,t}^{boiler} \cdot h_{in,t}^{boiler} = \dot{m}_{out,t}^{SC} \cdot h_{out,t}^{SC} + \dot{m}_{out,t}^{GFH} \cdot h_{out,t}^{GFH} \\ h_{out,t}^{boiler} = h_{in,t}^{SC} \\ h_{out,t}^{boiler} = h_{in,t}^{GFH} \end{cases} \quad \forall t \in T \quad (20)$$

In which the specific enthalpies of the heating fluid at the inlet and outlet of each solar thermal system equipment are estimated as follows.

$$h_t = Cp^{hf} \cdot T_t \quad \forall t \in T \quad (21)$$

In which, Cp^{hf} indicates the specific heat, and T_t the temperature of the heating fluid in the time period $t \in T$.

4.3.1. Solar Thermal Collectors

The thermal power produced by the solar collectors' field in the time period $t \in T$ is given by **Eq. (22)**.

$$1 \quad Q_t^{SC} = \dot{m}_{in,t}^{SC} \cdot (h_{out,t}^{SC} - h_{in,t}^{SC}) \quad \forall t \in T \quad (22)$$

2

3 The total area of the solar parabolic trough collectors is estimated as
4 follows.

5

$$6 \quad A^{SC} \geq \frac{Q_t^{SC}}{G_t \cdot \eta^{SC}} \quad \forall t \in T \quad (23)$$

7

8 In **Eq. (23)**, G_t is the daily solar radiation flux (irradiance) in the time period
9 $t \in T$. Also, η^{SC} is the thermal efficiency of the medium-high temperature solar
10 parabolic trough collectors as given by the following expression [25].

11

$$12 \quad \eta^{SC} = \eta_0 - a_1 \cdot (T_t^{avg} - T_t^{amb}) - a_2 \cdot \left(\frac{T_t^{avg} - T_t^{amb}}{G_t} \right) - a_3 \cdot \left(\frac{T_t^{avg} - T_t^{amb}}{G_t} \right)^2 \quad \forall t \in T \quad (24)$$

13

14 In which, η_0 is the collector optical efficiency, while a_1 , a_2 , and a_3 are
15 coefficients. T_t^{amb} and T_t^{avg} are the ambient and average temperatures in the time
16 period $t \in T$, respectively. The average temperature of the solar collectors is
17 calculated as follows.

18

$$19 \quad T_t^{avg} = 0.5 \cdot (T_{in,t}^{SC} + T_{out,t}^{SC}) \quad \forall t \in T \quad (25)$$

20

21 4.3.2. Gas-Fired Heater

22 The thermal power produced by the natural gas-fired heater in the time period
23 $t \in T$ is estimated as follows.

24

$$25 \quad Q_t^{GFH} = \dot{m}_t^{ng} \cdot LHV \cdot \eta^{GFH} \quad \forall t \in T \quad (26)$$

26

In which, \dot{m}_t^{ng} and LHV indicate the mass flowrate and lower heating value of natural gas, respectively. η^{GFH} is the thermal efficiency of the natural gas heater.

4.3.3. Boiler

The thermal power of the boiler in the time period $t \in T$ is given as follows.

$$Q_t^{boiler} = \dot{m}_{in,t}^{boiler} \cdot (h_{in,t}^{boiler} - h_{out,t}^{boiler}) \quad \forall t \in T \quad (27)$$

The heat transfer area of the boiler can be estimated by the following equation.

$$A^{boiler} = \frac{Q_t^{boiler}}{U^{boiler} \cdot LMTD_t^{boiler}} \quad (28)$$

In which, U^{boiler} indicates the heat transfer coefficient. The logarithmic mean temperature difference $LMTD_t^{boiler}$ in the time period $t \in T$ is obtained through the Chen's approximation [24]. In this case, the temperature differences are stated as follows.

$$\begin{cases} \theta_1 = T_{in,t}^{boiler} - T_{in}^{turbine} \\ \theta_2 = T_{out,t}^{boiler} - T_{out}^{RC-pump} \end{cases} \quad (29)$$

In which,

$$\begin{cases} T_{in,t}^{boiler} \geq T_{in}^{turbine} + \Delta T_{min} \\ T_{out,t}^{boiler} \geq T_{out}^{RC-pump} + \Delta T_{min} \end{cases} \quad (30)$$

4.4. Economic and Environmental Objective Functions

As mentioned before, the multi-objective NLP-based model is optimized via the simultaneous minimization of economic and environmental objective functions. These objective functions are presented in the following sections.

4.4.1. Economic Performance Evaluation

The economic objective function relates to minimizing the total annualized cost of the solar-assisted MEE-MVR system. The total annualized cost (TAC) is composed of the total capital investment ($CAPEX$) in all system devices, and total operating and maintenance expenses ($OPEX$) as stated as follows.

$$TAC = CAPEX + OPEX \quad (31)$$

The total capital investment comprises the costs of all equipment units from the MEE-MVR desalination system, steam Rankine cycle, and solar thermal system:

$$CAPEX = CAPEX^{MEE-MVR} + CAPEX^{RC} + CAPEX^{STS} \quad (32)$$

In which,

$$CAPEX^{MEE-MVR} = f_{ac} \cdot \left(\frac{CEPCI^{2019}}{CEPCI^{2003}} \right) \cdot \left[\left(C_{PO} \cdot F_{BM} \cdot F_P \right)^{evaporator} + \left(C_{PO} \cdot F_{BM} \cdot F_P \right)^{compressor} + \left(\sum_{i=1}^I C_{POi} \cdot F_{BM} \cdot F_P \right)^{flashing} + \left(C_{PO} \cdot F_{BM} \cdot F_P \right)^{preheater} \right] \quad (32a)$$

$$CAPEX^{RC} = f_{ac} \cdot \left(\frac{CEPCI^{2019}}{CEPCI^{2003}} \right) \cdot \left[\left(C_{PO} \cdot F_{BM} \cdot F_P \right)^{turbine} + \left(C_{PO} \cdot F_{BM} \cdot F_P \right)^{condenser} + \left(C_{PO} \cdot F_{BM} \cdot F_P \right)^{RC_Pump} \right] \quad (32b)$$

$$CAPEX^{STS} = f_{ac} \cdot \left(\frac{CEPCI^{2019}}{CEPCI^{2003}} \right) \cdot \left[\left(C_{PO} \cdot F_{BM} \cdot F_P \right)^{boiler} + \left(C_{PO} \cdot F_{BM} \cdot F_P \right)^{SC} + \left(C_{PO} \cdot F_{BM} \cdot F_P \right)^{GFH} + \left(C_{PO} \cdot F_{BM} \cdot F_P \right)^{STS_Pump} \right] \quad (32c)$$

1 In the previous formulation, f_{ac} represents the factor of cost annualization
 2 for the capital investment as described by Smith [26]:

$$3 \quad f_{ac} = \frac{f_i \cdot (1 + f_i)^y}{(1 + f_i)^y - 1} \quad (33)$$

5 In which, f_i indicates the fractional rate of interest per year, and y
 6 expresses the number of years in the considered period of amortization.
 7 Moreover, in **Eq. (32a) – Eq. (32c)**, C_{pO} represents the unitary cost of equipment
 8 (given in kUS\$) that operates at near-ambient pressure conditions. This unitary
 9 cost is obtained from cost correlations as proposed by Turton et al. [27] and
 10 Couper et al. [28]. In addition, F_{BM} is the correction factor of the basic unitary cost,
 11 which accounts for the operating pressure and construction materials. **Table 1**
 12 presents the correlations for unitary capital cost of equipment. Note that the total
 13 annualized cost should be adjusted for the reference year via the Chemical
 14 Engineering Plant Cost Index (CEPCI Index).

15 The operating and maintenance expenses encompasses the cost of utilities
 16 (e.g., natural gas, cooling water, and electricity), and equipment maintenance as
 17 stated as follows.

$$18 \quad OPEX = \left[\underbrace{C^{CW} \cdot Q^{condenser} + C^{electricity} \cdot \sum_{t \in T} W_t^{STS-pump} + C^{NG} \cdot \sum_{t \in T} Q_t^{GFH}}_{\text{operating expenses}} + \underbrace{0.25 \cdot CAPEX^{RC} + 0.15 \cdot CAPEX^{STS}}_{\text{equipment maintenance}} \right] \quad (34)$$

20 In which, C^{CW} , $C^{electricity}$, and C^{NG} are cost parameters for cooling water,
 21 electricity, and natural gas, respectively. In this study, the maintenance expenses
 22 of the Rankine cycle units are considered to be equal to 25% of the corresponding
 23 capital costs, while the maintenance expenses of the STS correspond to 15% of
 24 the capital costs of the same units.
 25

4.4.2. Environmental Performance Evaluation

The environmental objective function accounts for the environmental impacts associated with utilities consumption, which include electricity (STS pump), natural gas (GFH), and cooling water (condenser). In this study, the environmental impacts are quantified by the LCA-based ReCiPe methodology [29]. The quantification of environmental impacts is performed by LCA through four key stages. Firstly, the goal and scope are defined. The ReCiPe methodology accounts for 17 different categories of midpoint level impacts that are divided into three main damage groups at end level. Then, the Life Cycle Inventory (LCI) is carried out to appraise all material inputs and outputs, as well as energy inputs and outputs. In the third stage, the Life Cycle Impact Assessment (LCIA) is used to evaluate, weight and quantify the environmental impacts into eco-points. The environmental objective function is stated as follows.

$$EI = LCIA^{electricity} \cdot \sum_{t \in T} W_t^{STS_pump} + LCIA^{NG} \cdot \sum_{t \in T} Q_t^{GFH} + LCIA^{CW} \cdot Q^{condenser} \quad (35)$$

In which, $LCIA^{electricity}$, $LCIA^{NG}$, and $LCIA^{CW}$ denote the environmental impacts points (eco-points) related to the electricity used by the STS pump, natural gas consumed by the GFH, and cooling water required by the condenser, respectively. The environmental impacts are estimated through total ReCiPe points per year as obtained from the Ecoinvent database (Ecoinvent default, LCIA, ReCiPe Endpoint H/A, Europe/Es). A plant operating time of 8760 h/year is considered to convert original eco-points per energy production units into points per kW year units. The impacts associated with the stage of system construction are neglected as they are usually much smaller than those related to the operation during the system lifetime.

4.5. Optimization Procedure: Epsilon-Constraint Method

The multi-objective NLP problem can be formally expressed as follows.

$$\begin{aligned} \min \quad & \{TAC, EI\} \\ \text{s.t.} \quad & \text{all equality and inequality constraints} \end{aligned}$$

In which, TAC is given by **Eq. (31)**, while EI is estimated by **Eq. (35)**. The multi-objective mathematical model was implemented in GAMS software [30] (version 26.1.0), and solved via the epsilon-constraint method [31]. The epsilon-constraint method consists of formulating an auxiliary single-objective model, in which one objective is expressed as the main goal whilst the other objective is stated as an additional constraint. Then, the single-objective model is solved several times for different epsilon bound values that are imposed on the problem constraints. This approach allows obtaining a different optimal solution for each of the considered epsilon bound values. Hence, a Pareto curve can be constructed to show the set of alternative solutions, where each solution represents an optimal trade-off between the economic and environmental objective functions [32,33]. The local optimizer CONOPT4 was applied to optimize the multi-objective NLP problem with CPU time of ~2 min (180 different time periods and 30 Pareto-optimal solutions).

5. Case Study

A case study is presented to illustrate the effectiveness of the developed approach for the multi-objective optimization of solar-based ZLD desalination systems. The decentralized system is composed of an STS, Rankine cycle unit, and a ZLD-MEE-MVR desalination plant. **Fig. 1** depicts the schematic diagram for the solar-driven MEE-MVR system as proposed for the ZLD desalination of high-salinity shale gas wastewaters. The treatment capacity of the ZLD-MEE-MVR desalination plant is

1 equal to 10.42 kg/s of shale gas wastewater. The salt concentration (salinity) of
2 the feed water is 70 g/kg, and its inlet temperature is 25°C. For ensuring the ZLD
3 operation, the brine salinity should achieve a minimum value of 300 g/kg (300k
4 ppm) at the system discharge [34]. **Table 2** shows the process and cost
5 parameters used in the mathematical modelling formulation of the zero-liquid
6 discharge MEE-MVR system. Additional data encompass operational limitations
7 on the saturation pressure (200 kPa) and ideal temperature (100°C) to avoid
8 rusting and fouling-related issues in the evaporator unit [10,13]. The latter is
9 based on a horizontal-tube falling film configuration. Still, the evaporator unit is
10 built of nickel. A minimum temperature approach of 2°C is considered to prevent
11 temperature crossovers in the evaporator effects. Besides, minimum temperature
12 and pressure drops equal to 0.1°C and 0.1 kPa, respectively, are used between
13 two successive evaporation effects. The maximum compression ratio is limited to
14 3 in the mechanical vapor compressor (centrifugal/carbon steel), whilst the heat
15 capacity ratio is 1.33 [10,12,13].

16 In the STS, solar parabolic trough collectors are considered owing to their
17 greater efficiencies at high temperatures. The thermal fluid is Therminol 72 due
18 to its high thermal stability at temperatures up to 380°C [25]. The process and
19 cost parameters used for the optimal design of the steam Rankine cycle and STS
20 are presented in **Table 3**. The daily solar irradiance throughout the year in Spain
21 (N 41°7'8", E 1°14'43") is displayed in **Table 4**. The minimum temperature
22 difference in the hot end of the condenser is in a range of 5–15°C, while the
23 temperature increase of the thermal fluid in the boiler is 50°C. Cost parameters
24 include prices of electricity (812.47 US\$ per kW year), and natural gas (277.03 US\$
25 per kW year), which are retrieved from Eurostat database (2020). The factor of
26 annualized capital cost is equal to 0.163, which corresponds to 10% of interest
27 rate over 10 years of amortization period. **Table 5** presents the environmental
28 impact points of the utilities. The environmental impacts are estimated through
29 total ReCiPe points per year as obtained from the Ecoinvent database. A plant

1 operating time of 8760 h/year is considered to convert original ReCiPe eco-points
2 per energy production units into points per kW year units.

3 Firstly, the problem is solved by considering each optimization single-
4 objective alone. Thus, the optimization is performed via the minimization of the
5 total annualized cost (TAC), and the total environmental impacts (EI) separately.
6 Note that the minimization of the economic and environmental single-objectives
7 allows obtaining the limits of the epsilon-constraint interval. Then, the latter
8 interval is divided into a set of subintervals and successive optimizations
9 (iterations) are performed through the minimization of the economic objective-
10 function subjected to each environmental upper bound (*i.e.*, epsilon-constraint
11 that ensures that a given environmental limit is not exceeded). A set of optimal
12 trade-off Pareto solutions is then obtained by applying the previous epsilon-
13 constraint approach. The corresponding results are discussed as follows.

14 15 **6. Results and Discussion**

16 **6.1. Single-Objective Optimization: EI Minimization**

17 The total annualized cost obtained via the minimization of the environmental
18 objective-function is equal to 45592 kUS\$/year, encompassing 45433 kUS\$/year
19 associated with capital investment, and 159 kUS\$/year related to operating
20 (electricity, natural gas, and cooling water consumption) and maintenance
21 expenses. The capital cost is composed of 2603 kUS\$/year for the investment in
22 the MEE-MVR desalination system, and 42830 kUS\$/year for the STS and RC units.
23 Also, the total environmental impacts related to utilities consumption (electricity,
24 natural gas, and cooling water) are estimated to be ~193k ReCiPe eco-
25 points/year. This single-objective optimal solution corresponds to the extreme
26 solution referred to as "Design A" in **Fig. 2** and **Fig. 3**. In this case, the solar-based
27 desalination system requires a total area of the solar parabolic trough collectors

1 of $5.2 \times 10^5 \text{ m}^2$, and the RC steam turbine produces 502.49 kW of electricity to drive
2 mechanical compressor in the MEE-MVR plant.

3 The optimal ZLD-MEE-MVR system configuration achieved by the
4 environmental impacts minimization includes two different evaporation effects
5 with total heat transfer areas of 1268.94 m^2 and 468.64 m^2 . In addition, a feeding
6 preheater with a heat transfer area of 100.28 m^2 (1669.63 kW) is required in the
7 system, along with two flashing tanks with capacities of 2.39 m^3 and 1.19 m^3 . Note
8 that the capacity of the mechanical vapor compressor is equal to 502.49 kW.
9 Under this configuration, the desalination system achieves a freshwater
10 production ratio of 7.99 kg/s (i.e., ~77% of recovery of the total water amount
11 present in the wastewater).

12

13 **6.2. Single-Objective Optimization: TAC Minimization**

14 The total annualized cost obtained via the minimization of the economic
15 objective-function is equal to 2224 kUS\$/year, comprising 1794 kUS\$/year related
16 to capital investment, and 430 kUS\$/year associated with operating (electricity,
17 natural gas, and cooling water consumption) and maintenance expenses. The
18 capital cost is composed of 1166 kUS\$/year for the investment in the MEE-MVR
19 desalination system, and 628 kUS\$/year for the STS and RC units. Still, the total
20 environmental impacts related to utilities consumption (electricity, natural gas,
21 and cooling water) are estimated to be ~667.5k ReCiPe eco-points/year. This
22 single-objective optimal solution corresponds to the extreme solution referred to
23 as "Design B" in **Fig. 2** and **Fig. 3**. In this case, the solar-based desalination system
24 requires a total area of the solar parabolic trough collectors of 4942 m^2 , and the
25 RC steam turbine produces 734.68 kW of electricity to drive mechanical
26 compressor in the MEE-MVR plant.

27 The optimal configuration of the ZLD-MEE-MVR desalination system
28 obtained by the total annualized cost minimization encompasses two different
29 evaporation effects with total heat transfer areas of 284.54 m^2 and 297.22 m^2 . In

1 addition, a feeding preheater with a heat transfer area of 68.73 m² (1903.66 kW)
2 is required in the system, along with two flashing tanks with capacities of 2.39 m³
3 and 1.19 m³. Note that the capacity of the mechanical vapor compressor is equal
4 to 734.68 kW. Under this configuration, the desalination system achieves a
5 freshwater production ratio of 7.99 kg/s. The comparison between the two
6 extreme environmental and economic optimal solutions reveals that the total area
7 of heat transfer of the evaporator unit is reduced by ~66.5% when the total
8 annualized cost is minimized. Also, the total heat transfer area of the feed water
9 preheater is decreased in ~31.5%. Although the compressor capacity is increased
10 in ~46.2%, the minimization of the TAC leads to a reduction of ~55.2% in the
11 capital cost of the MEE-MVR when compared to the minimum EI solution. The
12 capital cost of investment in the STS and RC units is also decreased in ~98.5%,
13 which is mainly due to the reduction of ~99% in the total area of the solar
14 parabolic trough collectors. It should also be noted that the TAC is reduced in
15 ~95.1% while the EI is increased in 245.9%, when contrasting both extreme
16 optimal solutions.

17

18 **6.3. Multi-Objective Optimization: Pareto Optimal Solutions**

19 The Pareto set of optimal trade-off solutions obtained via the multi-objective
20 optimization procedure are displayed in **Fig. 2**. In this figure, Design A represents
21 the minimum EI solution while Design B indicates the minimum TAC solution. It
22 should be highlighted that each point in the Pareto curve correspond to an
23 optimal system design and associated process operating conditions, which yield
24 a unique combination of environmental and economic performance. Since a
25 given improvement in one criterion can only be attained at the expense of
26 impairing the another one, there is a clear trade-off between environmental and
27 economic objectives. Hence, the minimum EI solution (Design A) shows the worst
28 economic performance whilst the minimum TAC solution leads to the highest
29 environmental impacts. As mentioned before, the TAC of Design A is equal to

1 45592 kUS\$/year, whereas Design B presents a TAC of 2224 kUS\$/year. On the
2 other hand, it is also observed an increase in the environmental impacts from
3 ~193k to 667.5k points/year, when moving from Design A to Design B in the
4 Pareto curve.

5 A thorough examination of **Fig. 2** also reveals that the environmental
6 impacts are significantly reduced by increasing the area of the solar parabolic
7 trough collectors. However, as previously discussed, such EI reduction comes with
8 a considerable increase in the total annualized cost of the system. For further
9 analysis, the model is solved by fixing the solar collector area to zero. In this
10 solution, the TAC of the system is equal to 2243 kUS\$/year, whereas the EI are
11 estimated to be 992.3k points/year. The TAC is slightly higher than that of Design
12 B due to the increase in both the capital cost of investment in the MEE-MVR
13 desalination system, and operating expenses related to the larger consumption
14 of natural gas. Clearly, the latter result is also responsible for an increase of
15 ~48.7% in the environmental impacts of the system. Therefore, using solar
16 thermal collectors to drive the MEE-MVR desalination plant is not only an
17 environment-friendly solution but also an economically viable one.

18 Since Design A and Design B correspond to extreme solutions in the Pareto
19 Curve (which can be prohibitive either in terms of high process costs or excessive
20 environmental impacts), Design C can be identified as a promising alternative
21 optimal solution. In this case, the TAC of the system is equal to 6867 kUS\$/year,
22 while the total EI related to utilities consumption (electricity, natural gas, and
23 cooling water) is equal to 209.6k ReCiPe eco-points/year. Thus, it is possible to
24 decrease the TAC in ~85% at expense of only 8.5% of increase in environmental
25 impacts when moving from Design A to Design C. The decrease in the TAC is
26 mainly due to the reduction of total area of the solar parabolic trough collectors
27 from $5.2 \times 10^5 \text{ m}^2$ in point A to $4.3 \times 10^4 \text{ m}^2$ in point C. **Fig. 3** shows the dependence
28 of the TAC of the process on the total aperture area of the solar collectors (in log
29 scale) for each optimal design solution. Note that the energy required to drive

1 the ZLD-MEE-MVR desalination plant is fulfilled using primarily solar collectors in
2 Design A (minimum EI solution). In Design B and Design C, the energy demand is
3 covered by both the GFH and solar collectors. Moreover, the GFH is required in
4 all solutions (even in the minimum EI one) as a result of the solar energy
5 intermittency (particularly in night-time operation).

6 **Fig. 4** and **Fig. 5** depict the solar energy share of each optimal design in
7 different time periods during a day in January and July, respectively. January and
8 July are the months with the lowest and largest daily solar radiation flux
9 (irradiance) in the year, correspondingly. The solar fraction as portrayed in **Fig. 4**
10 and **Fig. 5** corresponds to the amount of energy required by the boiler in the STS
11 which is covered by solar collectors. In January, all energy demands of Design A
12 (minimum EI solution) are completely fulfilled by solar collectors in time periods
13 ranging from 7 to 17h. This is due to the large area of the solar collectors used in
14 this optimal solution. As a consequence of the highest solar irradiance in July, the
15 time periods in which all energy requirements of Design A are covered by solar
16 collectors are extended from 5 to 18h. Similar behaviors are observed for Design
17 C in the winter and summer days. However, Design C only requires 17.9% of solar
18 fraction in the time period 5-6h because of its low solar irradiance (and smaller
19 solar collectors' area). Note that in remaining hours of the day, the desalination
20 systems of Design A and Design C are completely operated by using natural gas
21 in the GFH. Since the solar collector area is significantly smaller in Design B
22 (minimum TAC solution), the solar energy shares are considerably reduced in this
23 solution. For instance, 82.3% of energy requirements of Design B in January are
24 fulfilled by solar collectors in peak solar irradiance periods (11-13h). Design B only
25 achieves 100% of solar fraction share in the peak solar irradiance periods of July.
26 Therefore, better advantage can be taken from the available solar irradiance by
27 increasing the solar collectors' area.

28 **Fig. 6** exhibits the costs breakdown (in log scale) for the different optimal
29 design solutions. The TAC of the Design C (6867 kUS\$/year) is comprised by 6721

1 kUS\$/year associated with capital investment in equipment, along with 146
2 kUS\$/year related to operating (electricity, natural gas, and cooling water
3 consumption) and maintenance expenses. As the ZLD-MEE-MVR desalination
4 plant of Design C is similar to that obtained in Design A (both designs present a
5 freshwater production ratio of 7.99 kg/s), both solutions present the same
6 corresponding capital cost of investment (2603 kUS\$/year). However, the capital
7 cost of investment in the STS is decreased by 90.4% as a result of the much smaller
8 solar collectors required in Design C. The environmental impacts breakdown (in
9 log scale) for the different design solutions are displayed in **Fig. 7**. As expected,
10 Design B shows the highest environmental impacts related to natural gas
11 consumption (~662k ReCiPe eco-points/year). The environmental impacts of
12 natural gas usage in Design B are ~71.4% higher than those in Design A.

13 **Fig. 8** and **Fig. 9** display the thermal power share in different time periods
14 in January and July, respectively. As shown in **Fig. 8 (a)**, the energy demands of
15 the boiler in Design B are covered by both the GFH and solar collectors in the
16 time periods ranging from 7 to 17h, while the corresponding energy requirements
17 are completely fulfilled by solar collectors in Design C. A similar behavior is
18 observed for Design B and Design C in time periods ranging from 6 to 18h of a
19 day in July (**Fig. 9 (a)** and **Fig. 9 (b)**, respectively). This is a result of the greater
20 solar collector's area required by solution C. Hence, even in the months of lower
21 solar irradiance, the energy performance of the system can be improved by
22 increasing the collectors' area. Although the latter can represent an increase in
23 the capital costs of the STS (84.7%), the natural gas consumption can be
24 significantly reduced as well as its corresponding environmental impacts (68.9%).
25 Noticeably, other alternative trade-off optimal solutions can be chosen in the
26 Pareto curve to reduce the capital costs required for solar collectors at expense
27 of small increases in environmental impacts. For that reason, the Pareto curve
28 obtained can be a valuable tool for supporting decision-makers towards

1 implementing more cost-effective and environment-friendly desalination systems
2 according to their preferences.

3

4 **7. Conclusions**

5 A new multi-objective model is developed for the thermo-economic and
6 environmental optimization of solar-driven ZLD systems, which are particularly
7 employed for desalinating high-salinity wastewaters from shale gas operations. A
8 decentralized ZLD system is proposed encompassing a solar thermal-assisted
9 Rankine cycle unit coupled to a MEE-MVR desalination plant. The solar thermal
10 system is designed for multi-period operation to account for the variation in the
11 daily solar irradiance during the year. Also, the ZLD operation of the desalination
12 plant is ensured by specifying the salinity of brine discharges close to saturation
13 conditions. The resulting multi-objective NLP model is implemented in GAMS and
14 solved by the epsilon-constraint method, via the minimization of both total
15 annualized costs and environmental impacts. The economic objective function
16 encompasses the capital investment of equipment, along with maintenance and
17 operating expenses related to utilities consumption. The environmental
18 performance is assessed by the ReCiPe methodology, which is based on LCA
19 techniques.

20 An illustrative case study centered on Spain's weather conditions is
21 performed to demonstrate the applicability of the proposed multi-objective
22 approach. A set of trade-off Pareto solutions is obtained revealing a reduction of
23 ~95.1% in the TAC at the expense of increasing environmental impacts in 245.9%,
24 when comparing minimum economic and environmental optimal solutions. The
25 Pareto curve also shows that intermediate optimal solutions provide significant
26 reductions in environmental impacts at small increases in the total costs. The
27 environmental impacts are mainly decreased by enlarging the area of the solar
28 parabolic trough collectors, which reduces the natural gas consumption and leads

1 to savings in operating expenses. Hence, the use of solar thermal collectors to
2 operate the ZLD-MEE-MVR desalination system can be not only an eco-friendly
3 alternative but also a cost-effectively solution. Thus, the comprehensive multi-
4 objective approach represents a useful tool able to identify the best alternatives
5 that simultaneous balance both environmental and economic criteria. For this
6 reason, the new multi-objective model can be used to support the decision-
7 making process towards implementing more sustainable and cost-efficient solar-
8 driven ZLD desalination systems. Future research will be focused on developing
9 new heat integration strategies to improve the overall system thermal efficiency.
10 Also, the critical aspects associated with the uncertain data will be utilized to
11 assess the most riskier decision-making attitudes.

1 **Acknowledgements**

2 This project has received funding from the European Union's Horizon 2020
3 Research and Innovation Programme under grant agreement No. 640979.

4

5

1 **Nomenclature**

2 *Acronyms*

3	BPE	Boiling Point Elevation
4	CEPCI	Chemical Engineering Plant Cost Index
5	CSP	Concentrated Solar Power
6	GAMS	General Algebraic Modelling System
7	GHF	Gas-fired Heater
8	LCA	Life Cycle Assessment
9	LCI	Life Cycle Inventory
10	LCIA	Life Cycle Impact Assessment
11	MD	Membrane Distillation
12	MEE	Multiple-Effect Evaporation
13	MED	Multiple-Effect Distillation
14	MVR	Mechanical Vapor Recompression
15	MSF	Multistage Flash Distillation
16	MoNLP	Multi-objective non-linear programming
17	NEA	Non-Equilibrium Allowance
18	NLP	Non-linear Programming
19	RC	Rankine Cycle
20	RO	Reverse Osmosis
21	STS	Solar Thermal System
22	ZLD	Zero-Liquid Discharge

23

24 *Roman letters*

25	A	Heat transfer area, m ²
26	BPE	Boiling point elevation, °C
27	C^{CW}	Parameter for cooling water cost, US\$/kW year
28	$C^{electricity}$	Parameter for electricity cost, US\$/kW year
29	C^{NG}	Parameter for natural gas cost, US\$/kW year

1	$CAPEX$	Capital investment, kUS\$/year
2	C_p	Specific heat, kJ/kg °C
3	CPO	Unitary cost of equipment, kUS\$
4	CR_{max}	Maximum ratio of compression
5	EI	Total environmental impact, points/year
6	f_{ac}	Annualized capital cost factor
7	FBM	Correction factor for the capital investment
8	f_i	Fractional rate of interest per year
9	FP	Parameter for capital investment estimation
10	G	Solar radiation flux (irradiance), kW/m ²
11	h	Specific enthalpy, kJ/kg
12	$LCIA$	Environmental impacts points, points/kW year
13	LHV	Lower heating value
14	$LMTD$	Logarithmic mean temperature difference
15	\dot{m}	Mass flowrate, kg/s
16	$OPEX$	Operational Expenses, kUS\$/year
17	P	Pressure, kPa
18	ΔP_{min}	Minimum pressure approach, kPa
19	Q	Heat flow, kW
20	rt	Retention time in the flashing tanks, min
21	S	Salinity, g/kg
22	s	Specific entropy, kJ/kg
23	T	Temperature, °C
24	TAC	Total annualized cost, kUS\$/year
25	ΔT_{min}	Minimum temperature approach, °C
26	U	Overall heat transfer coefficient, kW/m ² K
27	V	Volume of flashing tanks, m ³
28	X^{salt}	Mass fraction of salt

1	x	Vapor quality
2	W	Compression work, kW
3	y	Number of considered years
4		
5	<i>Subscripts</i>	
6	i	Evaporator effects
7	in	Stream inlet condition
8	out	Stream outlet condition
9	t	Time period
10		
11	<i>Superscript</i>	
12	amb	Ambient
13	avg	Average
14	cv	Condensate (or Distillate) vapor
15	CW	Cooling water
16	GFH	Gas-fired heater
17	IS	Isentropic
18	L	Liquid
19	mix	Mixture
20	ng	Natural gas
21	RC	Rankine Cycle
22	sat	Saturated vapor
23	SC	Solar collectors
24	STS	Solar thermal system
25	sup	Superheated vapor
26	V	Vapor
27		
28	<i>Greek letters</i>	
29	γ	Heat capacity ratio

1	η	Efficiency
2	θ	Temperature difference, °C
3	λ	Latent heat of vaporization, kJ/kg
4	ν	Specific volume
5	ρ	Density, kg/m ³
6		
7		

1 **References**

- 2 [1] J.A. Caballero, J.A. Labarta, N. Quirante, A. Carrero-Parreño, I.E. Grossmann,
3 Environmental and Economic Water Management in Shale Gas Extraction,
4 Sustainability. 12 (2020) 1686. doi:10.3390/su12041686.
- 5 [2] M. Thomas, T. Partridge, B.H. Harthorn, N. Pidgeon, Deliberating the
6 perceived risks, benefits, and societal implications of shale gas and oil
7 extraction by hydraulic fracturing in the US and UK, Nat. Energy. 2 (2017)
8 17054. doi:10.1038/nenergy.2017.54.
- 9 [3] G. Prpich, F. Coulon, E.J. Anthony, Review of the scientific evidence to
10 support environmental risk assessment of shale gas development in the UK,
11 Sci. Total Environ. 563–564 (2016) 731–740.
12 doi:10.1016/j.scitotenv.2015.11.026.
- 13 [4] NRC, Induced Seismicity Potential in Energy Technologies, National
14 Academies Press, Washington, D.C., 2013. doi:10.17226/13355.
- 15 [5] P.L. Staddon, M.H. Depledge, Fracking Cannot Be Reconciled with Climate
16 Change Mitigation Policies, Environ. Sci. Technol. 49 (2015) 8269–8270.
17 doi:10.1021/acs.est.5b02441.
- 18 [6] A. Samadi, H. Saidi, M.A. Latify, M. Mahdavi, Home energy management
19 system based on task classification and the resident’s requirements, Int. J.
20 Electr. Power Energy Syst. 118 (2020) 105815.
21 doi:10.1016/j.ijepes.2019.105815.
- 22 [7] A. Carrero-Parreño, V.C. Onishi, R. Ruiz-Femenia, R. Salcedo-Díaz, J.A.
23 Caballero, J.A. Reyes-Labarta, Optimization of multistage membrane
24 distillation system for treating shale gas produced water, Desalination. 460
25 (2019) 15–27. doi:10.1016/j.desal.2019.03.002.
- 26 [8] V.C. Onishi, E.S. Fraga, J.A. Reyes-Labarta, J.A. Caballero, Desalination of
27 shale gas wastewater: Thermal and membrane applications for zero-liquid
28 discharge, in: Emerg. Technol. Sustain. Desalin. Handb., Elsevier, 2018: pp.
29 399–431. doi:10.1016/B978-0-12-815818-0.00012-6.

- 1 [9] S.B. Kausley, C.P. Malhotra, A.B. Pandit, Treatment and reuse of shale gas
2 wastewater: Electrocoagulation system for enhanced removal of organic
3 contamination and scale causing divalent cations, *J. Water Process Eng.* 16
4 (2017) 149–162. doi:10.1016/j.jwpe.2016.11.003.
- 5 [10] V.C. Onishi, A. Carrero-Parreño, J.A. Reyes-Labarta, R. Ruiz-Femenia, R.
6 Salcedo-Díaz, E.S. Fraga, J.A. Caballero, Shale gas flowback water
7 desalination: Single vs multiple-effect evaporation with vapor
8 recompression cycle and thermal integration, *Desalination*. 404 (2017) 230–
9 248. doi:10.1016/j.desal.2016.11.003.
- 10 [11] H.R. Acharya, C. Henderson, H. Matis, H. Kommepalli, B. Moore, H. Wang,
11 Cost effective recovery of low-TDS frac flowback water for re-use, *Glob. Res.*
12 (2011) 1–100.
- 13 [12] V.C. Onishi, A. Carrero-Parreño, J.A. Reyes-Labarta, E.S. Fraga, J.A. Caballero,
14 Desalination of shale gas produced water: A rigorous design approach for
15 zero-liquid discharge evaporation systems, *J. Clean. Prod.* 140 (2017) 1399–
16 1414. doi:10.1016/j.jclepro.2016.10.012.
- 17 [13] V.C. Onishi, R. Ruiz-Femenia, R. Salcedo-Díaz, A. Carrero-Parreño, J.A.
18 Reyes-Labarta, E.S. Fraga, J.A. Caballero, Process optimization for zero-
19 liquid discharge desalination of shale gas flowback water under uncertainty,
20 *J. Clean. Prod.* 164 (2017) 1219–1238. doi:10.1016/j.jclepro.2017.06.243.
- 21 [14] EIA, U.S. Energy Information Administration. How much carbon dioxide is
22 produced per kilowatthour when generating electricity with fossil fuels?,
23 (2016).
- 24 [15] A.B. Pouyfaucou, L. García-Rodríguez, Solar thermal-powered desalination:
25 A viable solution for a potential market, *Desalination*. 435 (2018) 60–69.
26 doi:10.1016/j.desal.2017.12.025.
- 27 [16] S.E. Moore, S.D. Mirchandani, V. Karanikola, T.M. Nenoff, R.G. Arnold, A.
28 Eduardo Sáez, Process modeling for economic optimization of a solar
29 driven sweeping gas membrane distillation desalination system,

- 1 Desalination. 437 (2018) 108–120. doi:10.1016/j.desal.2018.03.005.
- 2 [17] V. Karanikola, S.E. Moore, A. Deshmukh, R.G. Arnold, M. Elimelech, A.E. Sáez,
3 Economic performance of membrane distillation configurations in optimal
4 solar thermal desalination systems, *Desalination*. 472 (2019) 114164.
5 doi:10.1016/j.desal.2019.114164.
- 6 [18] Y. Zheng, K.B. Hatzell, Technoeconomic analysis of solar thermal
7 desalination, *Desalination*. 474 (2020) 114168.
8 doi:10.1016/j.desal.2019.114168.
- 9 [19] M.M. Aboelmaaref, M.E. Zayed, J. Zhao, W. Li, A.A. Askalany, M. Salem
10 Ahmed, E.S. Ali, Hybrid solar desalination systems driven by parabolic
11 trough and parabolic dish CSP technologies: Technology categorization,
12 thermodynamic performance and economical assessment, *Energy Convers.*
13 *Manag.* 220 (2020) 113103. doi:10.1016/j.enconman.2020.113103.
- 14 [20] C. Ghenai, D. Kabakebji, I. Douba, A. Yassin, Performance analysis and
15 optimization of hybrid multi-effect distillation adsorption desalination
16 system powered with solar thermal energy for high salinity sea water,
17 *Energy*. 215 (2021) 119212. doi:10.1016/j.energy.2020.119212.
- 18 [21] A. Najafi, A. Jafarian, J. Darand, Thermo-economic evaluation of a hybrid
19 solar-conventional energy supply in a zero liquid discharge wastewater
20 treatment plant, *Energy Convers. Manag.* 188 (2019) 276–295.
21 doi:10.1016/j.enconman.2019.03.059.
- 22 [22] E. Lemmon, M. McLinden, D. Friend, *Thermophysical Properties of Fluid*
23 *Systems*, 1980.
- 24 [23] National Institute of Standards, *NIST Chemistry WebBook*, 2011.
- 25 [24] J.J.J. Chen, Comments on improvements on a replacement for the
26 logarithmic mean, *Chem. Eng. Sci.* 42 (1987) 2488–2489. doi:10.1016/0009-
27 2509(87)80128-8.
- 28 [25] R. Salcedo, E. Antipova, D. Boer, L. Jiménez, G. Guillén-Gosálbez, Multi-
29 objective optimization of solar Rankine cycles coupled with reverse osmosis

- 1 desalination considering economic and life cycle environmental concerns,
2 Desalination. 286 (2012) 358–371. doi:10.1016/j.desal.2011.11.050.
- 3 [26] R.M. Smith, Chemical Process Design and Integration, John Wiley & Sons
4 Ltd, England, 2005.
- 5 [27] R.C. Turton, Bailie, W.B. Whiting, J.A. Shaeiwitz, D. Bhattacharyya, Analysis,
6 Synthesis, and Design of Chemical Processes Fourth Edition, 2012.
- 7 [28] J.R. Couper, W.C. Penney, J.R. Fair, S.M. Walas, Chemical process equipment,
8 selection and design, Second Edition, Elsevier, USA, 2010.
- 9 [29] M. Goedkoop, R. Heijungs, M. Huijbregts, A. De Schryver, J. Struijs, R. Van
10 Zelm, ReCiPe 2008, Potentials. (2009) 1–44. [http://www.pre-](http://www.pre-sustainability.com/download/misc/ReCiPe_main_report_final_27-02-2009_web.pdf)
11 [sustainability.com/download/misc/ReCiPe_main_report_final_27-02-](http://www.pre-sustainability.com/download/misc/ReCiPe_main_report_final_27-02-2009_web.pdf)
12 [2009_web.pdf](http://www.pre-sustainability.com/download/misc/ReCiPe_main_report_final_27-02-2009_web.pdf).
- 13 [30] R.E. Rosenthal, GAMS — A User's Guide, GAMS Development Corporation,
14 Washington, DC, 2016.
- 15 [31] M. Ehrgott, Multicriteria optimization, Springer Verlag, New York, 2005.
- 16 [32] N. García, R. Ruiz-Femenia, J.A. Caballero, Teaching mathematical modeling
17 software for multiobjective optimization in chemical engineering courses,
18 Educ. Chem. Eng. 7 (2012) e169–e180. doi:10.1016/j.ece.2012.07.001.
- 19 [33] G. Mavrotas, Effective implementation of the ϵ -constraint method in Multi-
20 Objective Mathematical Programming problems, Appl. Math. Comput. 213
21 (2009) 455–465. doi:10.1016/j.amc.2009.03.037.
- 22 [34] D. Han, W.F. He, C. Yue, W.H. Pu, Study on desalination of zero-emission
23 system based on mechanical vapor compression, Appl. Energy. 185 (2017)
24 1490–1496. doi:10.1016/j.apenergy.2015.12.061.
- 25 [35] I.S. Al-Mutaz, I. Wazeer, Comparative performance evaluation of
26 conventional multi-effect evaporation desalination processes, Appl. Therm.
27 Eng. 73 (2014) 1194–1203. doi:10.1016/j.applthermaleng.2014.09.025.
- 28 [36] European Commission, Eurostat, (2016).
- 29

Appendix A. NLP Model for the Optimal MEE-MVR Design

A.1. Multiple-effect Evaporator Unit

The mass balances in the evaporator effect i can be expressed as follows.

$$\begin{cases} \dot{m}_{i+1}^{brine} = \dot{m}_i^{vapor} + \dot{m}_i^{brine} \\ \dot{m}_i^{brine} \cdot S_i^{brine} = \dot{m}_{i+1}^{brine} \cdot S_{i+1}^{brine} \end{cases} \quad \forall 1 \leq i \leq I-1$$
$$\begin{cases} \dot{m}_i^{feed_water} = \dot{m}_i^{vapor} + \dot{m}_i^{brine} \\ \dot{m}_i^{feed_water} \cdot S_{in}^{feed_water} = \dot{m}_i^{brine} \cdot S_i^{brine} \end{cases} \quad \forall i = I$$

The system operates under a backward feeding configuration. As a result, the brine salt concentration in the first evaporator effect $i = 1$ must match the ZLD design constraint (to ensure the ZLD operation), while salinity of the feed water (shale gas wastewater) is considered in the last effect $i = I$. For evaporation effects in between, that is $1 < i \leq I - 1$, brine is added as feeding stream. The global energy balances in evaporator effects $i \in I$ are given by **Eq. (A.2)**.

$$\begin{cases} Q_i + \dot{m}_{i+1}^{brine} \cdot h_{i+1}^{brine} = \dot{m}_i^{brine} \cdot h_i^{brine} + \dot{m}_i^{vapor} \cdot h_i^{vapor} & \forall i < I \\ Q_i + \dot{m}_{in}^{feed} \cdot h_i^{feed} = \dot{m}_i^{brine} \cdot h_i^{brine} + \dot{m}_i^{vapor} \cdot h_i^{vapor} & \forall i = I \end{cases} \quad (\text{A.2})$$

In which, Q_i indicates the heat flow supplied to system boundaries by the condensed vapor stream. The specific enthalpies of brine, feed water and boiling vapor streams are estimated via correlations as presented in the **Appendix B**. Note that brine and vapor are both at the same boiling temperature $T_i^{boiling}$ in the effect $i \in I$. The latter is evaluated by considering the boiling point elevation (BPE) over the ideal temperature in the evaporation effect i as follows.

$$T_i^{boiling} = T_i^{ideal} + BPE_i \quad \forall i \in I \quad (\text{A.3})$$

In which, BPE_i and ideal temperature T_i^{ideal} in the effect $i \in I$ are estimated by the correlations provided in the **Appendix B**. The energy requirements in evaporator effects $i \in I$ are given by the following equations.

$$\begin{cases} Q_i = \dot{m}^{sup} \cdot C_{P_i}^{vapor} \cdot (T^{sup} - T_i^{condensate}) + \dot{m}^{sup} \cdot (h_i^{cv} - h_i^{condensate}) + Q^{external} & \forall i = 1 \\ Q_i = \lambda_i \cdot (\dot{m}_{i-1}^{vapor} + \dot{m}_{c_{i-1}}^{vapor}) & \forall i > 1 \end{cases} \quad (\text{A.4})$$

In the evaporator effect $i = 1$, energy requirements embrace the sensible heat needed to achieve the outlet temperature of the condensate, and the latent heat of condensation of the superheated vapor. In other evaporator effects, the energy requirements are calculated by the latent heat of vaporization added to the effect by the flashed off condensate and boiling vapors. In **Eq. (A.4)**, $Q^{external}$ represents the energy from a steam external source that is used to avoid equipment oversizing. This energy amount is estimated as follows.

$$Q^{external} = \dot{m}^{steam} \cdot C_{P_i}^{vapor} \cdot (T^{steam} - T_i^{condensate}) + \dot{m}^{steam} \cdot (h_i^{cv} - h_i^{condensate}) \quad \forall i = 1 \quad (\text{A.5})$$

In **Eq. (A.5)**, the specific enthalpies for vapor h_i^{cv} and condensate $h_i^{condensate}$ phases are given by the correlations presented in the **Appendix B**. Note that the condensate temperature $T_i^{condensate}$ in effects $i \in I$ is obtained by considering the outlet vapor pressure of the mechanical compressor in the Antoine Equation (**Appendix B**).

In **Eq. (A.4)**, \dot{m}^{sup} is the superheated mass flowrate as given by the following equation.

$$\dot{m}^{sup} = \dot{m}_i^{vapor} + \dot{m}_{c_i}^{vapor} \quad \forall i = I \quad (\text{A.6})$$

1 In which, $\dot{m}_{c_i}^{vapor}$ and \dot{m}_i^{vapor} are mass flowrates of the flashed off and boiling
 2 vapor from the condensate in evaporator effects $i \in I$, correspondingly. The total
 3 evaporator heat transfer area is obtained by adding all effect areas as shown in
 4 the **Eq. (A.7)**.

$$6 \quad A^{evaporator} = \sum_{i=1}^I A_i \quad \forall i \in I \quad (A.7)$$

7
 8 In evaporator effect $i = 1$, the area of heat transfer corresponds to the sum
 9 of the areas associated with the latent and sensible heat transfer.

$$11 \quad A_i = \left[\dot{m}^{sup} \cdot C p_i^{vapor} \cdot (T^{sup} - T_i^{condensate}) / (U^S \cdot LMTD_i) + \right. \\ \left. \dot{m}^{sup} \cdot (h_i^{cv} - h_i^{condensate}) / U_i \cdot (T_i^{condensate} - T_i^{boiling}) \right] \quad \forall i = 1 \quad (A.8)$$

12
 13 For remaining evaporator effects, the following equation is used to
 14 estimate the heat transfer area:

$$16 \quad A_i = Q_i / (U_i \cdot LMTD_i) \quad \forall i > 1 \quad (A.9)$$

17
 18 In which, U_i is the overall heat transfer coefficient that is given by the
 19 following correlation [35].

$$21 \quad U_i = 0.001 \cdot \left[\frac{1939.4 + 1.40562 \cdot T_i^{boiling} - 0.00207525 \cdot (T_i^{boiling})^2}{0.0023186 \cdot (T_i^{boiling})^3} + \right] \quad \forall i \in I \quad (A.10)$$

22
 23 In **Eq. (A.9)**, $LMTD_i$ indicates the log mean temperature difference in
 24 evaporator effect $i \in I$. The latter is estimated by using the Chen's approximation
 25 [24] for avoiding numerical difficulties related to the temperature differences.

$$LMTD_i = \left[0.5 \cdot (\theta_{1i} \cdot \theta_{2i}) \cdot (\theta_{1i} + \theta_{2i}) \right]^{\frac{1}{3}} \quad \forall i \in I \quad (\text{A.11})$$

2

3 In which,

$$\theta_{1i} = \begin{cases} T_i^{\text{sup}} - T_i^{\text{boiling}} & \forall i=1 \\ T_i^{\text{sat}} - T_i^{\text{boiling}} & \forall i>1 \end{cases} \quad \theta_{2i} = \begin{cases} T_i^{\text{condensate}} - T_{i+1}^{\text{boiling}} & \forall i=1 \\ T_i^{\text{sat}} - T_{i+1}^{\text{boiling}} & \forall 1 < i < I \\ T_i^{\text{sat}} - T_i^{\text{feed}} & \forall i=I \end{cases} \quad (\text{A.12})$$

5

6 The following constraints are used to ensure the pressure feasibility in
7 evaporation effects $i \in I$.

8

$$\begin{aligned} P_i^{\text{vapor}} &\geq P_{i+1}^{\text{vapor}} + \Delta P_{\text{min}} \quad \forall i < I \\ P_i^{\text{vapor}} &= P_{i+1}^{\text{sat}} \quad \forall i < I \end{aligned} \quad (\text{A.13})$$

10

11 In which the vapor pressure P_i^{vapor} should equal the pressure of saturated
12 vapor from subsequent effect to avoid operating instabilities. Finally, the
13 following temperature constraints are considered to avoid temperature
14 crossovers in evaporator effects $i \in I$.

15

$$\left\{ \begin{aligned} T_i^{\text{sup}} &\geq T_i^{\text{condensate}} + \Delta T_{\text{min}}^1 & \forall i=1 \\ T_{i-1}^{\text{boiling}} &\geq T_i^{\text{condensate}} + \Delta T_{\text{min}}^1 & \forall i>1 \\ T_i^{\text{boiling}} &\geq T_{i+1}^{\text{boiling}} + \Delta T_{\text{min}}^2 & \forall i < I \\ T_i^{\text{boiling}} &\geq T_i^{\text{feed}} + \Delta T_{\text{min}}^2 & \forall i=I \\ T_i^{\text{condensate}} &\geq T_{i+1}^{\text{boiling}} + \Delta T_{\text{min}}^3 & \forall i < I \\ T_i^{\text{condensate}} &\geq T_i^{\text{feed}} + \Delta T_{\text{min}}^3 & \forall i=I \\ T_i^{\text{condensate}} &\geq T_i^{\text{boiling}} + \Delta T_{\text{min}}^4 & \forall i \in I \\ T_i^{\text{sat}} &\geq T_i^{\text{boiling}} + \Delta T_{\text{min}}^4 & \forall i \in I \end{aligned} \right. \quad (\text{A.14})$$

17

18

19

A.2. Flashing Tanks

The mass balances in the flashing unit of the evaporator effect i can be expressed as follows.

$$\begin{cases} \dot{m}^{sup} = \dot{m}_{c_i}^{vapor} + \dot{m}_{c_i}^{liquid} & \forall i = 1 \\ \dot{m}_{i-1}^{vapor} + \dot{m}_{c_{i-1}}^{vapor} + \dot{m}_{c_{i-1}}^{liquid} = \dot{m}_{c_i}^{vapor} + \dot{m}_{c_i}^{liquid} & \forall i > 1 \end{cases} \quad (\text{A.15})$$

In which, $\dot{m}_{c_i}^{vapor}$ and $\dot{m}_{c_i}^{liquid}$ represent the mass flowrates of vapor and liquid phases of the flashed off condensate in the effect $i \in I$, respectively.

The energy balances in the flashing unit of the evaporator effect i are given by the following equations.

$$\begin{cases} \dot{m}^{sup} \cdot h_i^{condensate} = \dot{m}_{c_i}^{vapor} \cdot h_{c_i}^{vapor} + \dot{m}_{c_i}^{liquid} \cdot h_{c_i}^{liquid} & \forall i = 1 \\ \left(\dot{m}_{i-1}^{vapor} + \dot{m}_{c_{i-1}}^{vapor} \right) \cdot h_i^{condensate} + \dot{m}_{c_{i-1}}^{liquid} \cdot h_{c_{i-1}}^{liquid} = \dot{m}_{c_i}^{vapor} \cdot h_{c_i}^{vapor} + \dot{m}_{c_i}^{liquid} \cdot h_{c_i}^{liquid} & \forall i > 1 \end{cases} \quad (\text{A.16})$$

In which, $h_{c_i}^{liquid}$ and $h_{c_i}^{vapor}$ indicate specific enthalpies of liquid and vapor states of the flashed off condensate in the effect $i \in I$, respectively.

The volume of the flashing unit of the evaporator effect i is determined by **Eq. (A.17)**.

$$\begin{cases} V_i^{flash} = \left(\dot{m}^{sup} \cdot rt \right) / \rho_i & \forall i = 1 \\ V_i^{flash} = \left(\dot{m}_{i-1}^{vapor} + \dot{m}_{c_{i-1}}^{liquid} \right) \cdot rt / \rho_i & \forall i > 1 \end{cases} \quad (\text{A.17})$$

In which, rt and ρ_i is the flashing tank retention time and condensate density, correspondingly. In this study, the retention time is considered to be 5 min.

1 **A.3. Mechanical Vapor Compressor**

2 The outlet isentropic temperature of the mechanical vapor compressor is given
3 as follows.

4

$$5 \quad T^{is} = (T_i^{mix} + 273.15) \cdot (P^{sup} / P_i^{vapor})^{\frac{\gamma-1}{\gamma}} - 273.15 \quad \forall i = I \quad (A.18)$$

6

7 In which, T_i^{mix} indicates the temperature of mixture obtained from an
8 energy balance of the mixer in the last evaporator effect $i = I$. P^{sup} is the pressure
9 of superheated vapor, which is limited by the maximum compression ratio CR_{max}
10 as follows.

11

$$12 \quad P^{sup} \leq CR_{max} \cdot P_i^{vapor} \quad \forall i = I \quad (A.19)$$

13

14 The temperature of the superheated vapor from the mechanical vapor
15 compressor is estimated as follows.

16

$$17 \quad T^{sup} = T_i^{mix} + \frac{1}{\eta^{IS}} \cdot (T^{IS} - T_i^{mix}) \quad \forall i = I \quad (A.20)$$

18

19 In which, η^{IS} represents the isentropic efficiency of the compressor. The
20 compressor mechanical power is given by the following equation.

21

$$22 \quad W^{compressor} = \dot{m}^{sup} \cdot (h^{sup} - h_i^{vapor}) \quad \forall i = I \quad (A.21)$$

23

24 In which, h^{sup} and h_i^{vapor} are specific enthalpies of vapor evaluated at
25 superheated and mixture temperatures, respectively. The correlations of vapor
26 specific enthalpies are shown in the **Appendix B**. The following constraints on

1 the superheated temperature and pressure are used to guarantee the proper
2 operation of the compressor.

3

$$\begin{aligned} T^{sup} &\geq T_i^{mix} & \forall i = I \\ P^{sup} &\geq P_i^{vapor} & \forall i = I \end{aligned} \quad (\text{A.22})$$

5

6 **A.4. Feed Water Preheater**

7 The energy balance in the feed water preheater unit is stated as follows.

8

$$9 \quad \dot{m}_{c_i}^{liquid} \cdot Cp_i^{condensate} \cdot (T_i^{ideal} - T_{out}^{freshwater}) = \dot{m}_{in}^{feed} \cdot Cp_{in}^{feed} \cdot (T_i^{feed} - T_{in}^{feed}) \quad \forall i = I \quad (\text{A.23})$$

10

11 In which, T_{in}^{feed} and $T_{out}^{freshwater}$ are temperatures of the feed water and
12 produced freshwater by the system, correspondingly.

13 The total heat transfer area of the feed water preheater is given by **Eq.**
14 **(A.24)**.

15

$$16 \quad A^{preheater} = \dot{m}_{c_i}^{liquid} \cdot Cp_i^{condensate} \cdot (T_i^{ideal} - T_{out}^{freshwater}) / (U \cdot LMTD) \quad \forall i = I \quad (\text{A.24})$$

17

18 In which, U represents the overall heat transfer coefficient at T_i^{ideal} as
19 estimated by **Eq. (A.10)**.

20

21 **A.5. Zero-Liquid Discharge Specification**

22 The zero-liquid discharge operation of the thermal desalination system is ensured
23 by the following design constraint.

24

$$25 \quad S_i^{brine} \geq S^{design} \quad \forall i = 1 \quad (\text{A.25})$$

26

1 **Appendix B. Thermodynamic Correlations**

2 The thermodynamic correlations to estimate the boiling point elevation (BPE), and
3 the fluid physical properties are presented as follows.

4

5 **B.1. Boiling Point Elevation**

6 The BPE corresponds to the raise in the temperature of boiling point triggered by
7 the salt concentration of brine. The BPE in evaporation effect i is estimated by
8 the following equation.

9

$$10 \quad BPE_i = \left(\begin{array}{l} 0.1581 + 2.769 \cdot X_i^{salt} - 0.002676 \cdot T_i^{ideal} \\ + 41.78 \sqrt{X_i^{salt}} + 0.134 \cdot X_i^{salt} \cdot T_i^{ideal} \end{array} \right) \quad \forall i \in I \quad (B.1)$$

11 Where,

$$12 \quad X_i^{salt} = 0.001 \cdot S_i^{brine} \quad \forall i \in I \quad (B.2)$$

13

14 In **Eq. (B.1)**, T_i^{ideal} is the ideal temperature ($^{\circ}\text{C}$) and X_i^{salt} the mass fraction
15 of salt in the evaporator effect $i \in I$. The ideal temperature is the theoretical
16 temperature that a stream would assume if its salt concentration was equal to
17 zero. In **Eq. (B.2)**, S_i^{brine} is the brine salinity in the effect $i \in I$.

18

19 **B.2. Physical Properties of Fluids**

20 The thermodynamic properties of fluids in each evaporation effect are estimated
21 via correlations obtained from Aspen HYSYS-OLI. The process simulations have
22 been performed by using the electrolytes thermodynamic package. The
23 thermodynamic correlations for properties estimation are presented as follows.
24 They are valid for temperatures between 10°C to 120°C , and salt concentrations
25 in a range of 0 to 0.3.

26

27

1 B.2.1. Specific Enthalpy

2 The specific enthalpies of liquid and vapor states of fluids in the evaporation effect
3 i are given by the following correlations.

4

$$5 \quad h_i^{liquid} = -15940 + 8787 \cdot X_i^{salt} + 3.557 \cdot T_i^{boiling} \quad \forall i \in I \quad (B.3)$$

$$6 \quad h_i^{vapor} = -13470 + 1.840 \cdot T_i^{boiling} \quad \forall i \in I \quad (B.4)$$

7

8 In which, $T_i^{boiling}$ represents the boiling temperature in effect $i \in I$ given in
9 °C. To evaluate the specific enthalpies of condensate flows, the salt
10 concentrations are taken equal to zero, together with the corresponding
11 temperature $T_i^{condensate}$ in **Eq. (B.3)**. The specific enthalpy of the feed salt water is
12 also obtained by **Eq. (B.3)** by taking the appropriate salt mass fraction (X_{in}^{feed}) and
13 temperature (T_{in}^{feed}).

14

15 B.2.2. Latent Heat of Vaporization

16 The vaporization latent heat of streams in the evaporation effect i is given as
17 follows.

18

$$19 \quad \lambda_i = 2502.5 - 2.3648 \cdot T_i^{sat} + 1.840 \cdot (T_{i-1}^{sat} - T_i^{sat}) \quad \forall i > 1 \quad (B.5)$$

20

21 In which, T_i^{sat} indicates the temperature of the saturated vapor in effect
22 $i \in I$ expressed in °C. The saturated vapor temperature is estimated via the
23 Antoine Equation for vapor-liquid equilibrium as shown in **Eq. (B.6)**.

24

$$25 \quad \ln(P_i^{sat}) = A + \frac{B}{(T_i^{sat} + C)} \quad \forall i \in I \quad (B.6)$$

26

1 In which, P_i^{sat} represents the streams saturation pressure (given in kPa).
 2 Furthermore, A , B , and C refer to the parameters in Antoine equation of 12.98437,
 3 -2001.77468, and 139.61335, correspondingly. **Eq. (B.6)** can also be used to
 4 estimate the ideal temperature T_i^{ideal} in evaporation effect $i \in I$. In this case, the
 5 pertaining pressure of vapor (P_i^{vapor}) should be considered in **Eq. (B.6)**.

6

7 *B.2.3. Specific Heat*

8 The specific heat of the feed water in the last evaporation effect $i = I$ is given as
 9 follows.

10

$$11 \quad C_{p_{in}^{feed}} = 0.001 \cdot \left[\begin{array}{l} 4206.8 - 6.6197 \cdot S_{in}^{feed} + 1.2288e^{-2} \cdot (S_{in}^{feed})^2 + \\ (-1.1262 + 5.418e^{-2} \cdot S_{in}^{feed}) \cdot T_{in}^{feed} \end{array} \right] \quad (B.7)$$

12

13 The specific heat of the condensate can be obtained by considering the
 14 stream salinity equal to zero in **Eq. (B.7)**. Thus,

15

$$16 \quad C_{p_i^{condensate}} = 0.001 \cdot (4206.8 - 1.1262 \cdot T_i^{ideal}) \quad \forall i = I \quad (B.8)$$

17

18

19

20

21

22

List of Figure Captions

Fig. 1. Schematic diagram for the solar-based zero-liquid discharge desalination system. GFH, gas-fired heater; MEE-MVR, multiple-effect evaporation with mechanical vapor recompression.

Fig. 2. Pareto set of optimal trade-off solutions. Design A indicates the minimum environmental impact solution, while Design B represents the minimum total annualized cost solution.

Fig. 3. Dependence of the total annualized cost of the process on the total aperture area of the solar collectors (log scale).

Fig. 4. Solar energy share in different time periods during a winter day in January.

Fig. 5. Solar energy share in different time periods during a summer day in July.

Fig. 6. Breakdown of the total annualized cost (log scale) for the different design solutions. CAPEX_{des}, capital cost of the MEE-MVR desalination system; CAPEX_{solar}, capital cost of the solar thermal system and Rankine cycle units; OPEX, operational and maintenance expenses.

Fig. 7. Breakdown of the environmental impacts (log scale) for the different design solutions. EI, environmental impacts.

Fig. 8. Thermal power share in different time periods during a winter day in January for (a) Design B (minimum total annualized solution); and, (b) Design C (intermediate optimal solution).

Fig. 9. Thermal power share in different time periods during a summer day in July for (a) Design B (minimum total annualized solution); and, (b) Design C (intermediate optimal solution).

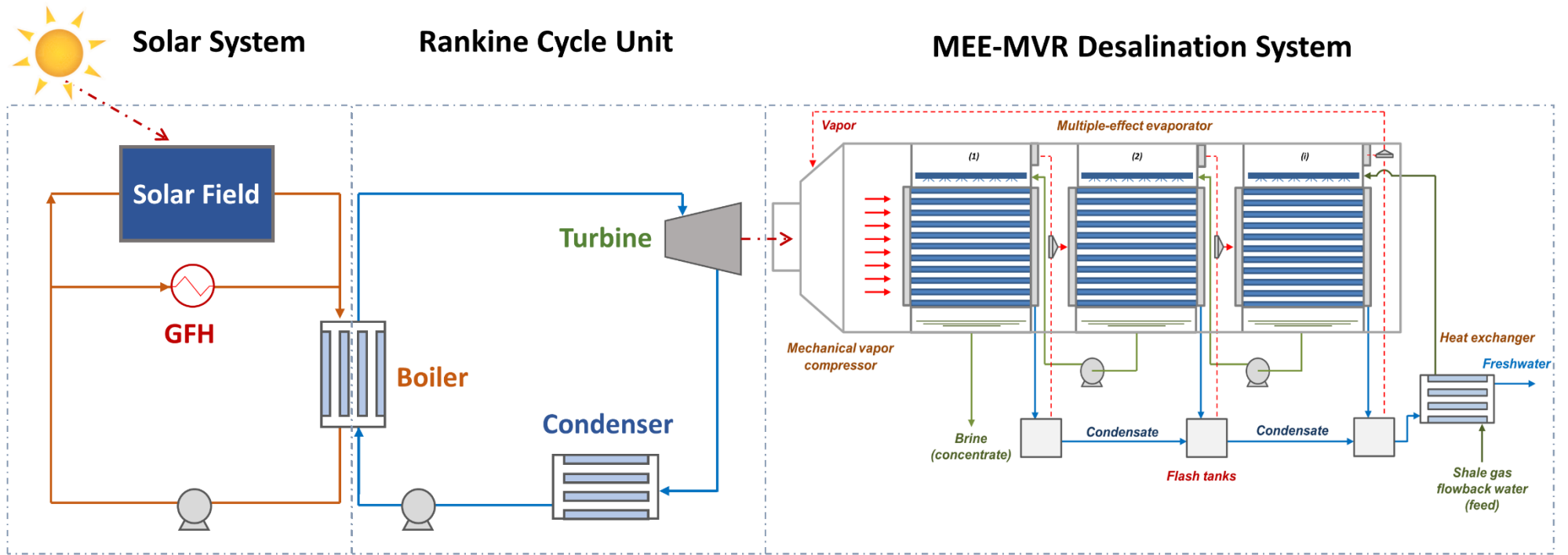


Fig. 1. Schematic diagram for the solar-based zero-liquid discharge desalination system. GFH, gas-fired heater; MEE-MVR, multiple-effect evaporation with mechanical vapor recompression.

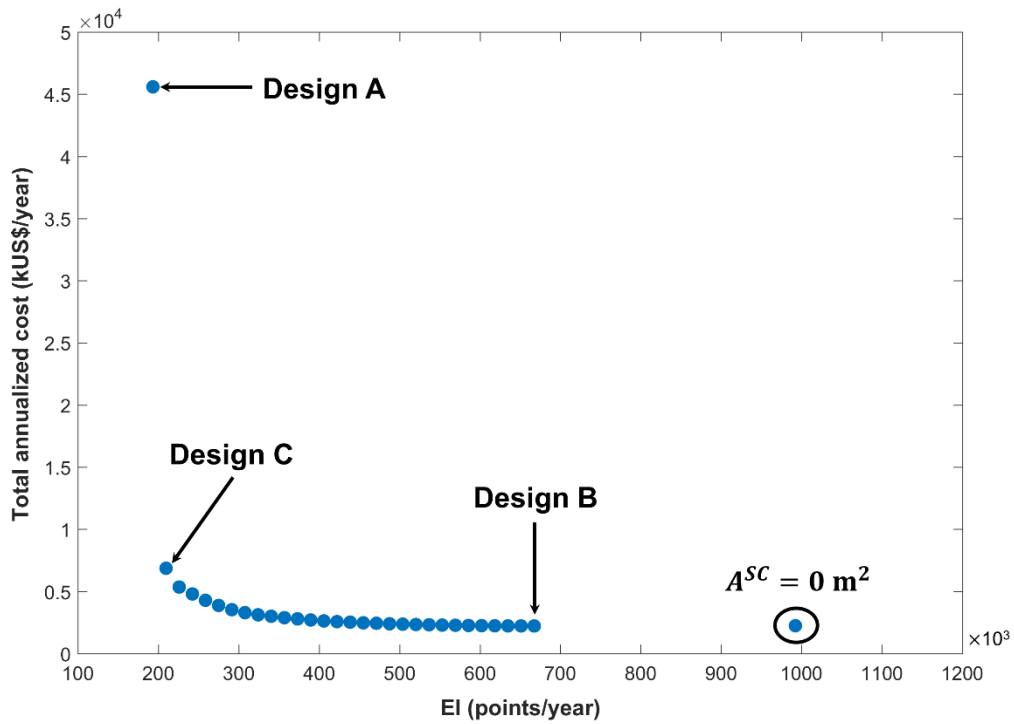


Fig. 2. Pareto set of optimal trade-off solutions. Design A indicates the minimum environmental impact solution, while Design B represents the minimum total annualized cost solution.

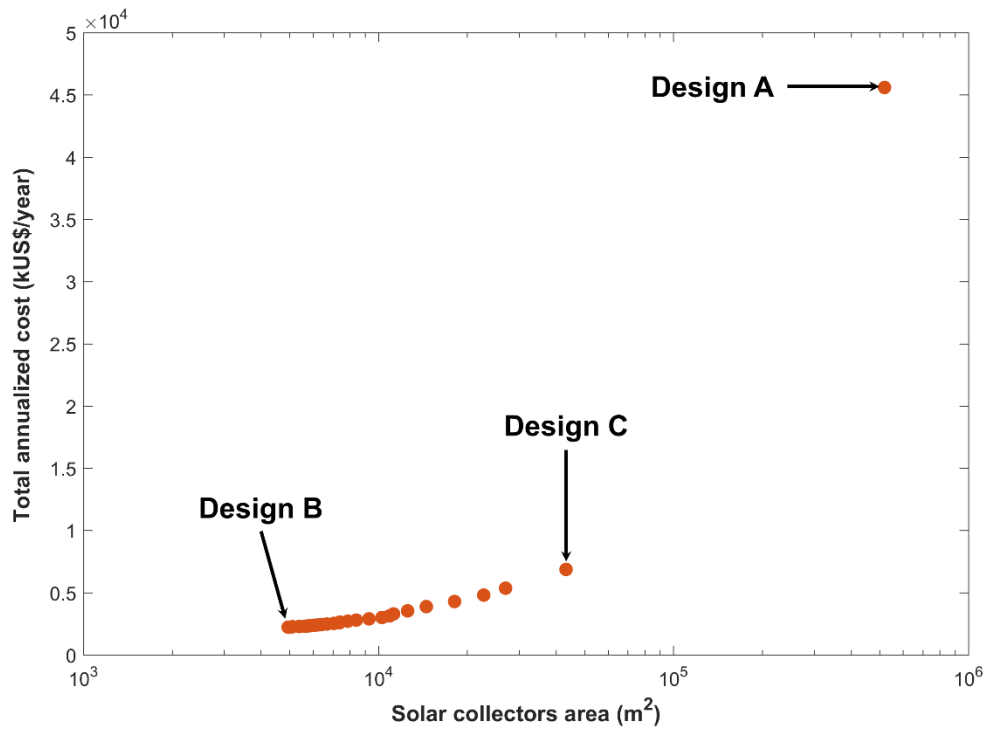


Fig. 3. Dependence of the total annualized cost of the process on the total aperture area of the solar collectors (log scale).

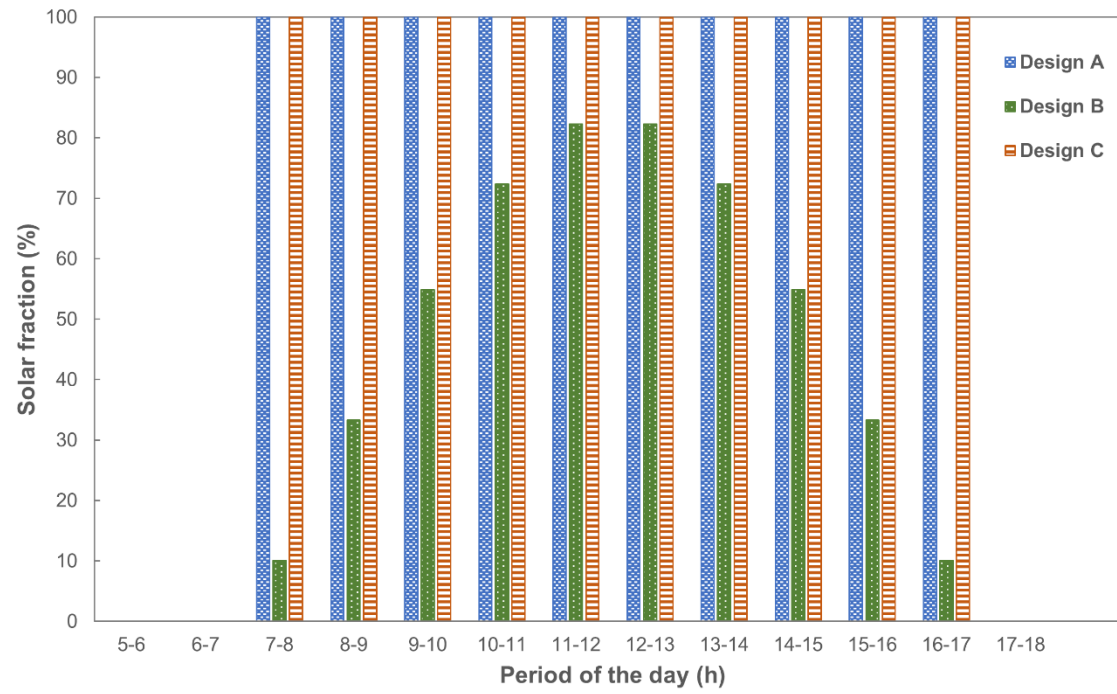


Fig. 4. Solar energy share in different time periods during a winter day in January.

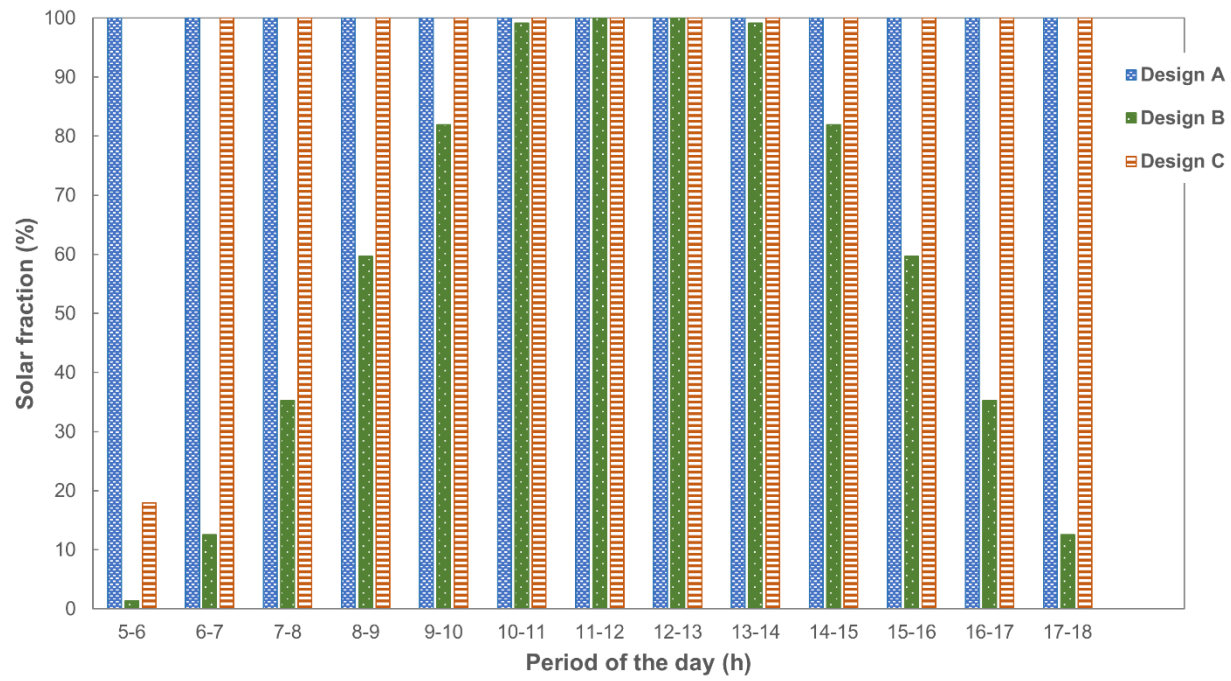


Fig. 5. Solar energy share in different time periods during a summer day in July.

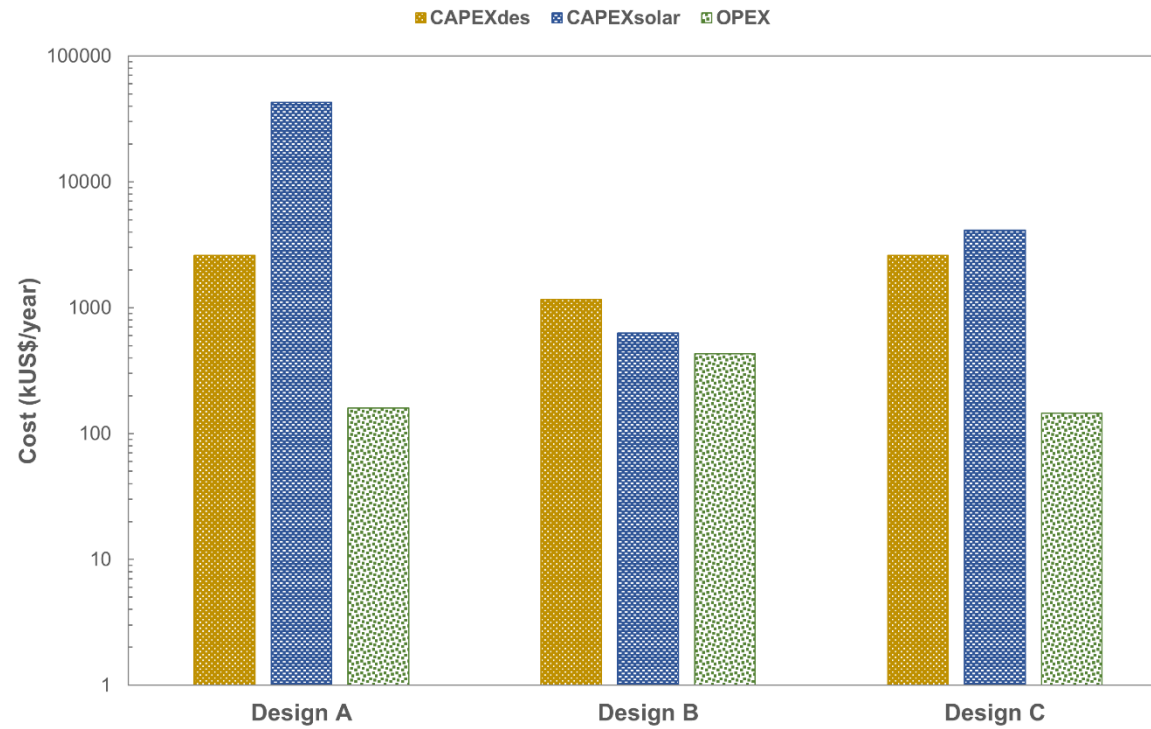


Fig. 6. Breakdown of the total annualized cost (log scale) for the different design solutions. CAPEXdes, capital cost of the MEE-MVR desalination system; CAPEXsolar, capital cost of the solar thermal system and Rankine cycle units; OPEX, operational and maintenance expenses.

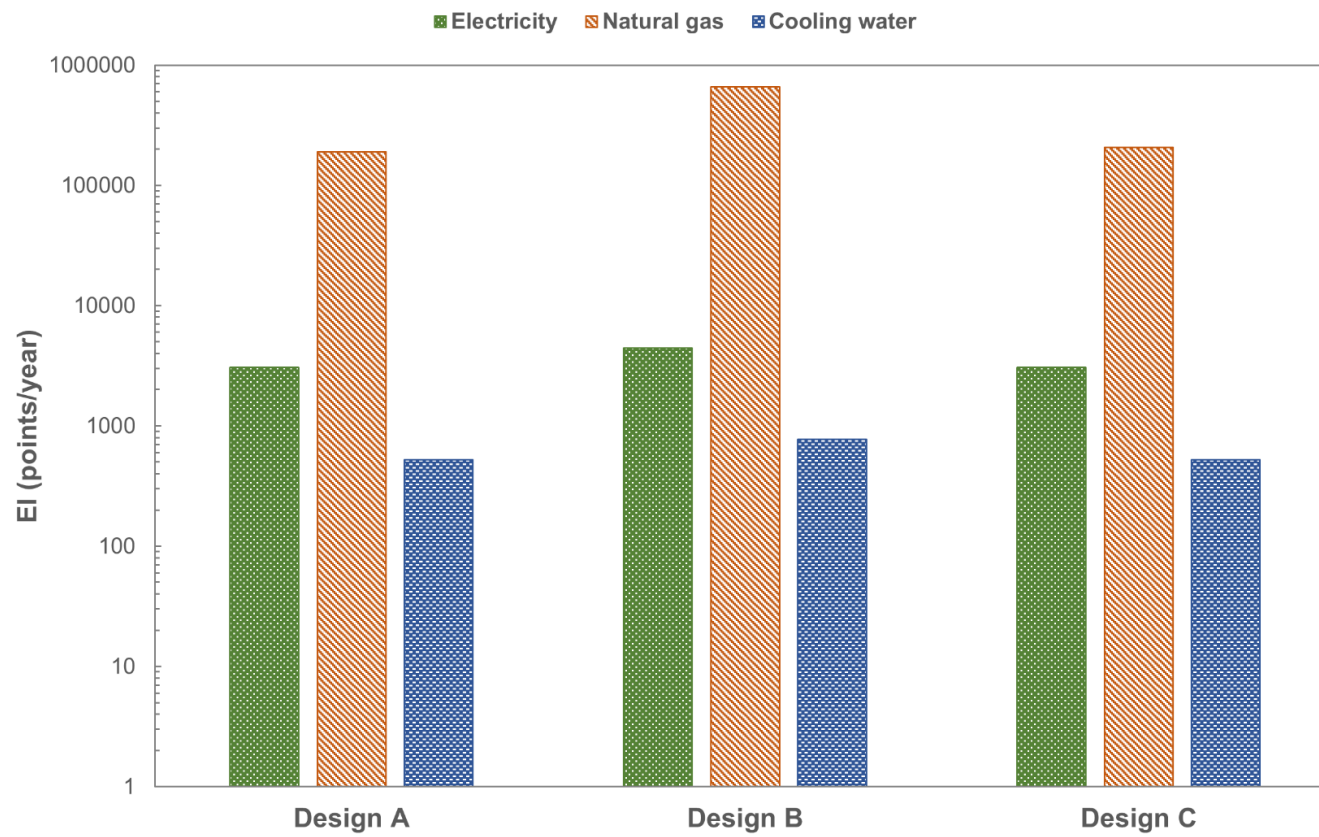


Fig. 7. Breakdown of the environmental impacts (log scale) for the different design solutions. EI, environmental impacts.

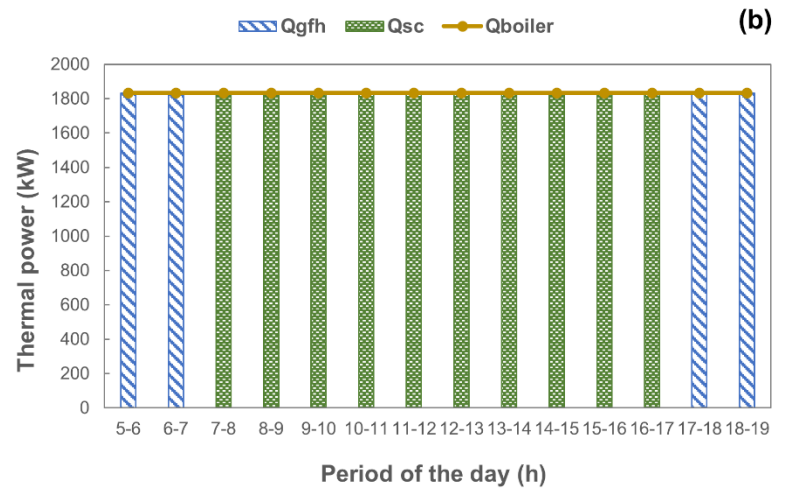
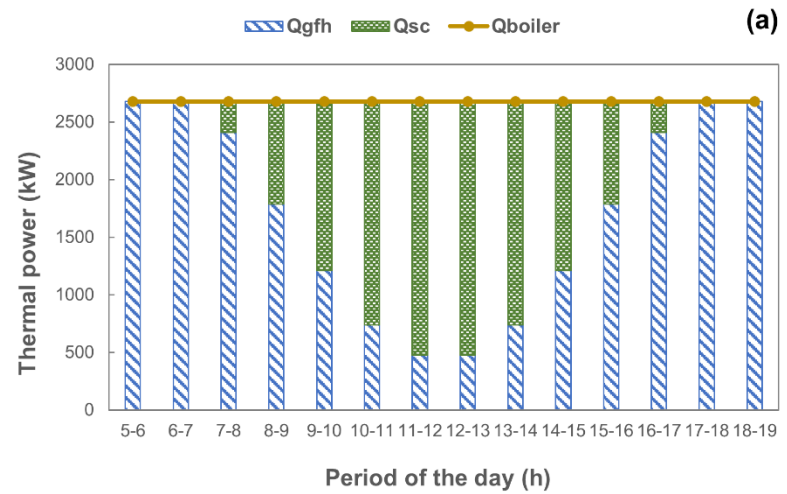


Fig. 8. Thermal power share in different time periods during a winter day in January for (a) Design B (minimum total annualized solution); and, (b) Design C (intermediate optimal solution).

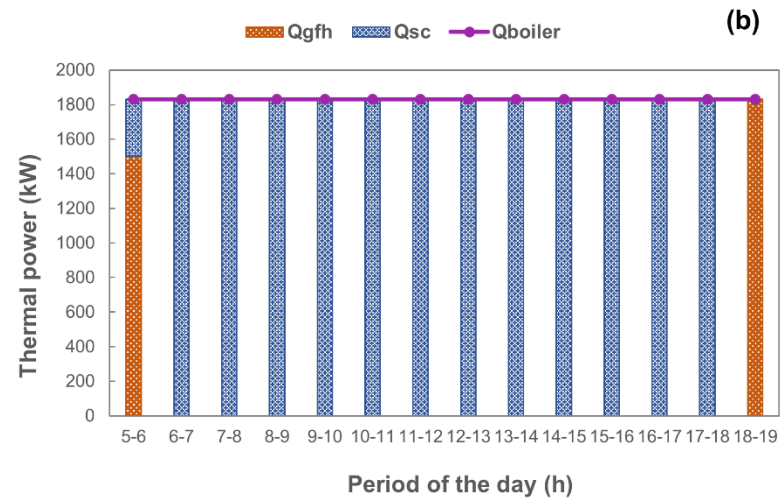
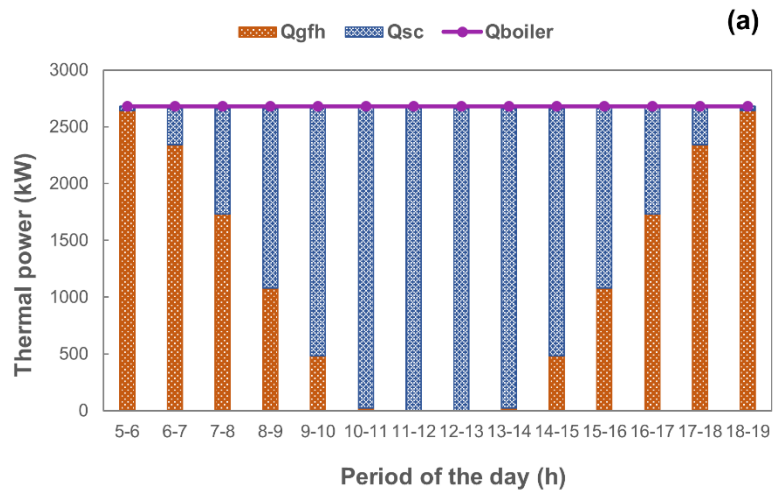


Fig. 9. Thermal power share in different time periods during a summer day in July for (a) Design B (minimum total annualized solution); and, (b) Design C (intermediate optimal solution).

Table 1

Correlations for unitary capital cost of equipment (given in kUS\$) [27,28].

Equipment	C_{PO}	F_{BM}
Multi-effect evaporator	$C_{PO} = 2.898 \cdot \sum_i A_i + 159.8$	1.8
Mechanical vapor compressor	$C_{PO} = 7.9 \cdot (W^{compressor} / 0.7457)^{0.62}$	2.2
Flashing tank	$C_{PO} = 6.554 \times 10^{-3} \cdot \sum_i (V_i^{flash})^2 + 0.8219 \cdot \sum_i V_i^{flash} + 3.557$	4.07
Preheater	$C_{PO} = 0.11479 \cdot A^{preheater} + 13.597$	3.95
RC Turbine	$C_{PO} = 0.378 \cdot (W^{turbine} / 0.7457)^{0.81}$	2.2
Condenser	$C_{PO} = 0.11479 \cdot A^{condenser} + 13.597$	3.95
RC Pump	$C_{PO} = 0.795 \cdot (W^{RC_pump})^{0.52}$	1
Boiler	$C_{PO} = 0.11479 \cdot A^{boiler} + 13.597$	3.95
Solar collectors	$C_{PO} = 0.6395 \cdot (A^{SC})^{0.95}$	1
Gas-fired heater	$C_{PO_i} = 3.325 \times 10^{-2} \cdot (Q_i^{GFH})^{0.82}$	1

Table 2

Parameters used in the mathematical model for the optimal design of the zero-liquid discharge MEE-MVR system.

Feed water	Mass flowrate, \dot{m}_i^{feed} (kg/s)	10.42
	Temperature, T_i^{feed} (°C)	25
	Salinity, $S_{in}^{feed_water}$ (g/kg or k ppm)	70
Mechanical vapor compressor	Isentropic efficiency, η^{is} (%)	75
	Heat capacity ratio, γ	1.33
	Maximum compression ratio, CR_{max}	3
Process specification and operating constraints	Salinity of ZLD operation, S^{design} (g/kg or k ppm)	300
	Maximum temperature, T_i^{ideal} (°C)	100
	Maximum pressure, P_i^{sat} (kPa)	200
	Number of evaporation effects	2
Economic data	Electricity price ¹ , $C^{electricity}$ (US\$/kW year)	812.47
	Fractional interest rate per year, fi	0.1
	Amortization period, y	10
	Working hours per year, (h)	8760

¹ Cost data obtained from Eurostat database [36] (1st semester – 2020).

Table 3

Parameters used in the mathematical model for the optimal design of the steam Rankine cycle and solar thermal system [7,25,27].

Rankine cycle	Turbine isentropic efficiency, η^{IS} (%)	78
	Specific heat of water vapor, C_p (kJ/kg K)	2.7
	Inlet cooling water temperature, T_{in}^{CW} (K)	298
	Outlet cooling water temperature, T_{out}^{CW} (K)	308
Solar collectors	Collector optical efficiency, η_0 (%)	75
	Solar collector constant, a_1	4.5e-6
	Solar collector constant, a_2	0.039
	Solar collector constant, a_3	3e-4
	Specific heat of the thermal fluid (Therminol 72), C_p^{hf} (kJ/kg K)	2.528
Gas-fired heater	Efficiency, η^{GFH} (%)	75
	Lower heating value of natural gas, LHV (kJ/kg)	47100
Pump	RC pump efficiency, $\eta^{RC-pump}$ (%)	60
	Specific volume of working fluid, ν (m ³ /kg)	1.2e-3
Economic data	Natural gas price ¹ , C^{NG} (US\$/kW year)	277.03
	Cooling water cost (US\$/kW year)	11.16
	Fractional interest rate per year, f_i	0.1
	Amortization period, y	10
	Working hours per year, (h)	8760

¹ Cost data obtained from Eurostat database [36] (1st semester – 2020).

Table 4Daily solar radiation flux (irradiance)¹ throughout the year [25].

Month	5-6	6-7	7-8	8-9	9-10	10-11	11-12	12-13	13-14	14-15	15-16	16-17	17-18	18-19
<i>January</i>	0.00	0.00	92.78	260.28	416.67	543.89	615.28	615.28	543.89	416.67	260.28	92.78	0.00	0.00
<i>February</i>	0.00	0.00	155.83	322.22	488.06	621.67	696.39	696.39	621.67	488.06	322.22	155.83	0.00	0.00
<i>March</i>	0.00	57.50	211.11	387.78	559.17	695.56	771.39	771.39	695.56	559.17	387.78	211.11	57.50	0.00
<i>April</i>	3.61	90.00	253.89	433.89	604.44	743.33	816.94	816.94	743.33	604.44	433.89	253.89	90.00	3.61
<i>May</i>	25.28	106.94	272.22	448.06	615.00	741.67	811.11	811.11	741.67	615.00	448.06	272.22	106.94	25.28
<i>June</i>	34.17	112.50	276.94	452.22	611.39	733.61	800.28	800.28	733.61	611.39	452.22	276.94	112.50	34.17
<i>July</i>	30.00	109.44	274.44	450.83	611.94	736.11	803.89	803.89	736.11	611.94	450.83	274.44	109.44	30.00
<i>August</i>	13.89	97.22	261.11	438.61	609.44	740.00	811.39	811.39	740.00	609.44	438.61	261.11	97.22	13.89
<i>September</i>	0.00	70.83	226.67	402.78	571.94	705.83	785.56	785.56	705.83	571.94	402.78	226.67	70.83	0.00
<i>October</i>	0.00	0.00	173.61	341.11	506.67	639.17	713.06	713.06	639.17	506.67	341.11	173.61	0.00	0.00
<i>November</i>	0.00	0.00	112.50	270.56	425.56	551.39	621.94	621.94	551.39	425.56	270.56	112.50	0.00	0.00
<i>December</i>	0.00	0.00	70.28	235.83	386.67	510.00	579.44	579.44	510.00	386.67	235.83	70.28	0.00	0.00

¹ Irradiance values given in kW/m²

Table 5

Environmental impact points of the utilities.

Utility	Process	Total ReCiPe eco-points (points/kW year)
Electricity	Electricity, production mix ES	949.32
Natural gas	Natural gas, burned in industrial furnace > 100 kW	454.49
Cooling water	Tap water production, underground water with chemical treatment	0.396